Level densities, thermodynamics and the γ-ray strength functions in ^{163,164}Dy

Master Thesis
Hilde-Therese Nyhus
Institute of Physics, University of Oslo

June 2008

Acknowledgments

After two years as a master student at the nuclear physics group, there are many people who have helpt me on the way and who deserves acknowledgment. First and foremost I am very thankful for having Sunniva Siem as my supervisor. She is a skilled nuclear physicist and a great teacher, who has inspired and motivated me throughout this work. Secondly I owe many thanks to Magne Guttormsen, Ann-Cecilie Larsen and Naeem Ul Hasan Syed for also being very helpful and who have always taken time out of what they are doing to help me whenever I have needed it. I must also mention that all of you along with the rest of the group and the group of SAFE have made the social environment very pleasant and this has made these years very enjoyable.

Last but not least I would like to say thanks to all my family and friends for being supportive. Thereby most of all my brothers Sverre-Kjetil and Helge-Jacob for all their encouragement, and for taking care of things allowing me to focus fully on my thesis.

For this study I was given a data set which reviled both interesting and some surprising results. This have made this work fun, interesting and very learning. For this I am very grateful.

Hilde-Therese Nyhus

June 2, 2008

Contents

1 Introduction **1**

2 Level density, thermodynamics and γ -ray strength function **4**
2.1 Level density 4
2.2 Thermodynamic properties derived from the level density 6
2.2.1 The micro-canonical ensemble 6
2.2.2 The canonical ensemble 8
2.3 The γ-ray strength function 9
2.3.1 Pygmy resonance 9
2.3.2 Giant electric and magnetic dipole resonance 10

3 Experimental method and data analysis **13**
3.1 Experimental details and detector setup 13
3.2 Signal treatment 15
3.3 Particle identification 15
3.4 The time spectrum 18
3.5 The particle spectra 20
3.6 The γ spectra 22
3.7 Unfolding the γ-ray spectra 22
3.7.1 The response function 23
3.7.2 Folding iteration method 25
3.7.3 The Compton subtraction method 26

4 The Oslo method **29**
4.1 The first generation matrix 29
4.2 The Brink-Axel hypothesis 34
4.3 Normalizing the level density 36
4.4 Normalizing the γ-transmission coefficient 40

5 Experimental level density and thermodynamic properties 44
5.1 The experimental level density 44
5.2 Experimental thermodynamic properties 47
5.3 Micro-canonical ensemble 48
5.3.1 Entropy 48
5.3.2 Temperature 50
5.3.3 Heat capacity 51
5.4 Canonical ensemble 53
5.4.1 Entropy 53
5.4.2 Energy 54
5.4.3 Heat capacity 54
5.5 Comparison of the ensembles 56

6 Experimental results on the γ-ray strength function 57
6.1 The predicted γ-ray strength function fitted to experimental data . 57
6.2 Including one extra Lorenzian function in the predicted γ-ray strength function 63
6.3 Comparing with results obtained from the two-step cascade method 66
6.4 Transferred angular momentum 66

7 Summary and outlook 69
7.1 Summary and conclusions 69
7.2 Outlook 70

List of Figures

1.1 Gamma-ray strength function of several rare earth isotopes studied at the OCL 2

2.1 Illustration of the scissor more 10
2.2 Illustration of the giant electric dipole resonance 11

3.1 Schematic drawing of the CACTUS multidetector array 14
3.2 Particle identification 17
3.3 Thickness spectrum 18
3.4 Time spectrum 19
3.5 Alpha-spectra 21
3.6 The ^{3}He-spectra 21
3.7 Gamma-spectra for ^{163}Dy 22
3.8 Gamma-spectra for ^{164}Dy 23
3.9 Illustration of the interpolation of the Compton background 25
3.10 Unfolded, folded and raw γ spectra for ^{163}Dy 27

4.1 Illustration of the method used to extract the primary γ-rays 30
4.2 First generation matrix obtained for ^{163}Dy 33
4.3 First generation matrix obtained for ^{164}Dy 34
4.4 Statistical decay in the continuum energy region 35
4.5 Level density adjusted to known energy levels in ^{163}Dy 38
4.6 Level density adjusted to known energy levels in ^{164}Dy 38
4.7 Level density adjusted to neutron resonance spacing data in ^{163}Dy 39
4.8 Level density adjusted to neutron resonance spacing data in ^{164}Dy 39
4.9 Gamma-ray transmission coefficient for ^{163}Dy 42
4.10 Gamma-ray transmission coefficient for ^{164}Dy 42

5.1 Experimental level density for ^{163}Dy 45
5.2 Experimental level density for ^{164}Dy 46
5.3 Entropies obtained from the micro-canonical ensemble 48
5.4 The entropy difference obtained from the micro-canonical ensemble 49

5.5 Temperature of ^{163}Dy obtained from the micro-canonical ensemble 50
5.6 Temperature of ^{164}Dy obtained from the micro-canonical ensemble 51
5.7 Heat capacity of ^{163}Dy obtained from the micro-canonical ensemble 52
5.8 Heat capacity of ^{164}Dy obtained from the micro-canonical ensemble 52
5.9 Entropies obtained from the canonical ensemble 53
5.10 Average excitation energies obtained from the canonical ensemble 55
5.11 Heat capacities obtained from the canonical ensemble 55

6.1 Gamma-ray strength function for ^{163}Dy fitted with the 3 MeV pygmy resonance 60
6.2 Gamma-ray strength function for ^{164}Dy fitted with one pygmy resonance at temperature $T = 0.3$ MeV 61
6.3 Gamma-ray strength functions for ^{160,161,162}Dy 62
6.4 Gamma-ray strength function for ^{163}Dy fitted with two pygmy resonance 64
6.5 Gamma-ray strength function for ^{164}Dy fitted with two pygmy resonance 65

List of Tables

4.1 Parameters used for the level density with the back shifted Fermi gas model 40
4.2 Parameters used to normalize the γ-transmission coefficient 43

6.1 Parameters used in the KMF model for the GEDR. 59
6.2 Lorentz parameters used for the GMDR 59
6.3 Fitted pygmy-resonance parameters and normalization constants of the 3 MeV pygmy resonance 59
6.4 Fitted pygmy-resonance parameters and normalization constants for ^{160,161,162}Dy 59
6.5 Fitted pygmy-resonance parameters and normalization constants of the first of two pygmy resonance 63
6.6 Angular momentum transfer with different beams 68

Chapter 1

Introduction

From the very beginning of nuclear physics a continuing effort has been devoted to study γ-decay from excited nuclei. Information on γ-decay has been accumulated almost exclusively for low lying nuclear levels with excitation energy, typically not exceeding $2-3$ MeV for medium heavy nuclei. Above this region the number of levels increases so much that a quasi-continuum is reached. Little experimental data are collected from this region up to the neutron binding energy. One exception is experiments performed by use of the Oslo method.

Average properties of γ-decay in the quasi-continuum are described by the level density and the γ-ray strength function. The level density and the γ-ray strength function give rich information about the nuclei. These quantities are of interest both in nuclear physics as well as in other branches of physics. One of the applications of level density is to extract thermodynamic properties of the nucleus. It is also used as an input in astrophysical models of the nucleosynthesis in stars. The γ-ray strength function describes electromagnetic properties of the nucleus. By use of the Oslo method we are able to extract both the level density and the γ-ray strength function from one and the same experiment [1]. The Oslo group has in recent years worked with mapping the level density and γ-ray strength function for several nuclei. Most of the nuclei studied belong to the group of rare earth isotopes, that is, nuclei with mass number in the range $A = 140-180$. In the present work we will continue this mapping by investigating two dysprosium isotopes, namely ^{163,164}Dy. These are medium heavy, well deformed rare earth nuclei in the mid-shell region.

In this thesis we are particularly interested in a resonance in the γ-ray strength function in the 3 MeV region. This originates from the so-called scissor mode, which has been shown by the Oslo group to be an M1 mode of the nucleus [2], also shown in Ref. [3]. This mode, called the 3 MeV pygmy resonance, appears as a bump in the γ-ray strength function. It has been observed for several rare

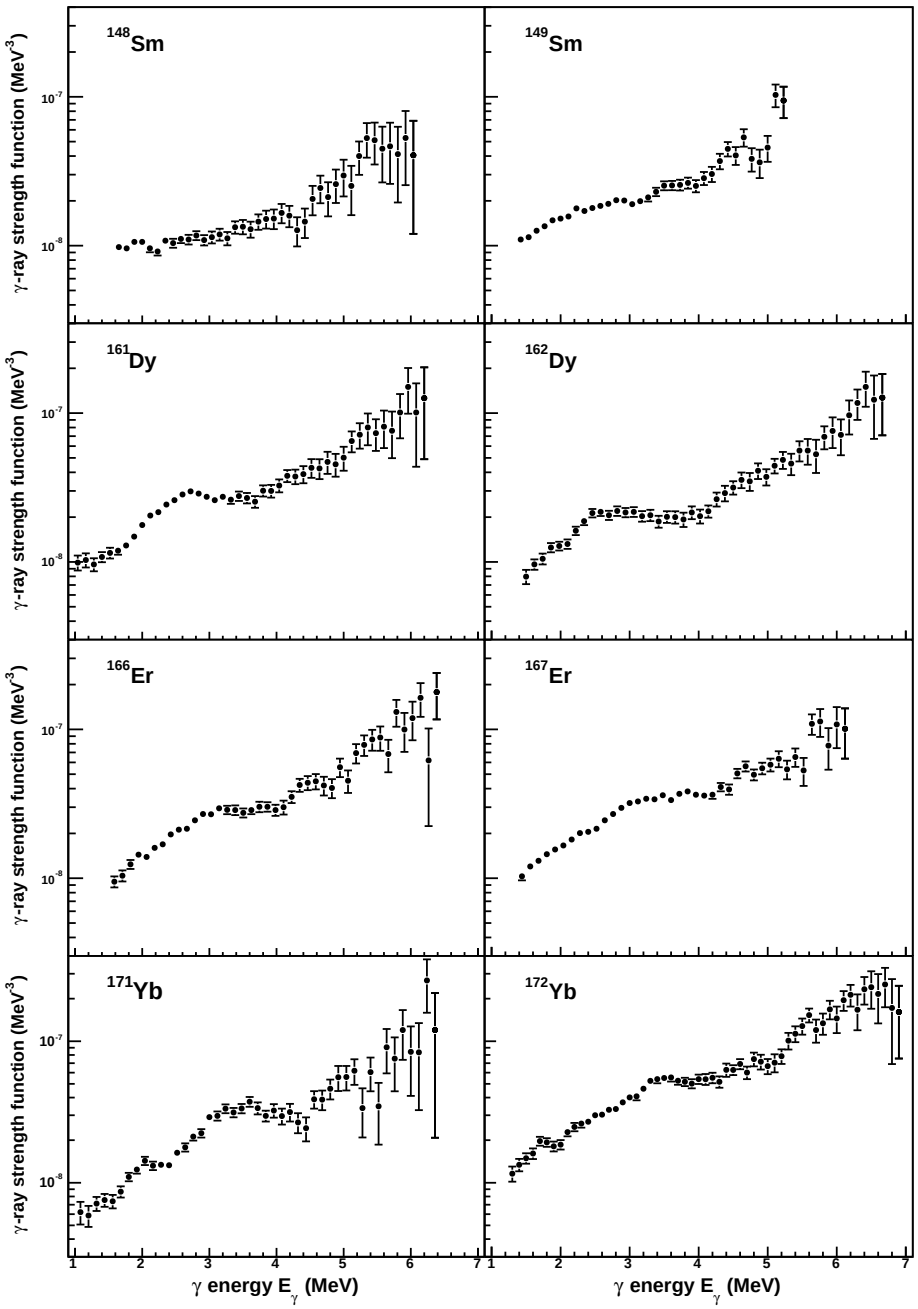

Figure 1.1: *Gamma-ray strength function of several rare earth isotopes studied at OCL. We observe the* 3 *MeV pygmy resonance in all of the strength functions displayed above, besides samarium. It is not present in samarium due to shell effects in this nucleus. The data is taken from: URL: http://ocl.uio.no/compilation/*

earth isotopes, some of them are displayed in Fig. 1.1. The width of the resonance have been measured to lie in the interval $0.84 - 1.57$ MeV for the dysprosium nuclei previously studied at the Oslo Cyclotron Laboratory (OCL) [4]. Of the main motivation for the current study is to investigate the width of the pygmy resonance in ^{163,164}Dy. The width will be compared to results found for ^{163}Dy [3] obtained with the so-called two step cascade (TSC) method [5]. Through this method one has measured a considerable smaller width of the pygmy resonance in ^{163}Dy, than what is observed in other dysprosium isotopes by use of the Oslo method. Through the present analysis we will be able to conclude if there are reaction dependent parameters that influence the width. Secondly we want to extract the level density and thermodynamic properties, and see if they coincide with previously observations for other dysprosium isotopes as well as for other rare earth nuclei.

In chapter 2 the theory behind the level density, how to extract thermodynamic properties from the level density, and the theory behind the γ-ray strength function will be presented. In chapter 3 experimental details and the data analysis are described. Chapter 4 is dedicated to the Oslo method, and the level density and thermodynamic properties achieved from this method is presented in chapter 5. In chapter 6 the experimental γ-ray strength function is discussed and compared to previous experiments at the OCL and to results found from the TSC method. Finally, a summary and conclusion of this analysis is given in chapter 7.

Chapter 2

Level density, thermodynamics and γ -ray strength function

The main goal with the present analysis as well as for previous experiments performed at the OCL is to extract the level density and the γ-ray strength function. In this chapter we will look into the information obtained from these measurements, and why they are so significant.

2.1 Level density

The level density gives the number of levels per energy unit as a function of excitation energy. At low excitation energy the level density is directly obtained by counting low-lying levels. As the excitation energy increases the level density becomes large and individual levels are often not resolved in experiments. It is said that the level density has reached the quasi-continuum. Where the quasi-continuum region starts differs for different nuclei, in rare earth isotopes it is typically reached above a few MeV of excitation energy. The level density together with the γ-ray strength function are used to calculate nuclear reaction cross sections. Knowledge about the cross sections are necessary to calculate astrophysical reaction rates and for modeling nucleosynthesis in stars. It is also important with respect to nuclear reactors and waste management. In addition we are able to extract thermodynamic properties from the level density, as will be described in the next section.

Bethe developed the so called Fermi gas model in 1936 [6], which gives the level density as function of excitation energy. The original formula is given by

$$\rho(E) = \frac{\sqrt{\pi}}{12} \frac{\exp(2\sqrt{aE})}{a^{1/4}E^{5/4}}, \tag{2.1}$$

at an given excitation energy E. The level density parameter a is expressed by

$$a = \frac{\pi}{6}(g_p + g_n), \tag{2.2}$$

where g_p and g_n are the single-particle level density parameters for protons and neutrons, respectively. There are weaknesses in this model because particles are assumed to move independently, and single particle states are considered to be equally spaced. Due to this, the Fermi gas model does not account for odd-even and collective effects. Later modified versions of the Fermi gas formula has been developed, where these effects are accounted for by employing free parameters that are adjusted to fit the experimental data on level spacings obtained from neutron or proton resonance experiments. Gilbert and Cameron developed in 1965 a level density formula where the effective excitation energy is reduced by the pairing energy for the odd-mass and even-even nuclei [7], resulting in a lower level density for the same excitation energy. Later it has been shown that the shift equal to $\Delta_p + \Delta_n$ is to large and it is 'back-shifted' by subtracting a parameter C_1 [8]. The most recent back-shifted Fermi gas model was developed by Egidy and Bucurescu [9] in 2005. It is given by the following expression

$$\rho_{BS}(E) = \frac{\exp[2\sqrt{a(E-E_1)}]}{12\sqrt{2}\sigma a^{1/4}(E-E_1)^{5/4}}, \tag{2.3}$$

for an excitation energy E, where the level density parameter a and the energy shift E_1 are treated as free parameters to be fitted to experimental data. Sigma is the spin-cutoff parameter, equal to the mean value of the spin distribution at a given excitation energy. It is expressed as

$$\sigma^2 = 0.0146A^{5/3}\frac{1+\sqrt{1+4a(E-E_1)}}{2a}, \tag{2.4}$$

where A denotes the mass number.

In addition to the Fermi gas model there exist a variety of other models that can be used to calculate the level density. However, for the medium heavy, mid-shell nuclei, as will be studied in this work, there are many degrees of freedom and a corresponding high level density. As a results it is hard to perform calculations on these nuclei with the present models. However, attempts have been made, perhaps the most successful one is by use of the shell model Monte Carlo method, which has been applied to calculate level densities [10, 11, 12] even for some dysprosium isotopes [13].

2.2 Thermodynamic properties derived from the level density

In microscopic systems such as the atomic nucleus , any attempt to measure thermodynamic properties by equipment like for example a thermometer, would of course not work because of the size of the system. However, the level density $\rho(E)$ can be used to derive various thermodynamic properties through statistical models. To understand this, we will first discuss some basic principles of statistical mechanics.

In the present case we have a microscopic system consisting of 163 and 164 nucleons for ^{163}Dy and ^{164}Dy, respectively. These nucleons can be arranged in different ways which result in different observed properties. We would therefore like to study the probability distribution of these configurations. We know that at thermodynamic equilibrium for an isolated system all available microscopic states are equally likely. The number of these states increases with excitation energy, and for nuclei similar to those we are studying the number of states per excitation energy reaches a quasi-continuum for energies above a few MeV. From the density of states $\Omega_s(E)$ all other thermodynamic quantities can be obtained. The density of states $\Omega_s(E)$ is directly proportional to the level density and a spin dependent factor [14]

$$\Omega_s(E) \propto \rho(E)(2\langle J(E)\rangle + 1), \tag{2.5}$$

where $\langle J(E)\rangle$ is the average spin at excitation energy E. There exist little experimental data on the spin distribution, therefore we will in this analysis work with a multiplicity $\Omega(E)$ that is based on the level density alone,

$$\Omega(E) \propto \rho(E). \tag{2.6}$$

The level density is through Eq. (2.6) our basic quantity for collecting information about the thermodynamics of the nucleus. However, one must keep in mind that the thermodynamic properties derived in this thesis are "pseudo" quantities, because we do not take into consideration the spin dependence.

Care has to be taken when choosing the ensemble that best describes the system. It is not quite obvious which ensemble is the most correct to use. In the following sections the micro-canonical and canonical ensemble will be described.

2.2.1 The micro-canonical ensemble

The micro-canonical ensemble is the assembly of many isolated systems with fixed total energy E, and fixed size V. One usually applies the micro-canonical

ensemble when describing a nucleus. One can justify this because the nuclear force has a very short range, and the nucleus does normally not share its excitation energy with its surroundings. It is therefore fair to consider the nucleus as an isolated system. However, the drawback for applying this ensemble is that some thermodynamic properties, such as the temperature T and heat capacity C_V, can have huge fluctuations and even negative values.

Among the important characteristics of a system is its entropy S. The entropy of a system is the measure of the disorder or randomness of the system. The second law of thermodynamics states that the entropy is an increasing function as a function of energy. The maximization of entropy ensures that the system strives to reach equilibrium, which corresponds to the most probable configuration of the system. The entropy can be expressed through the density of states. The definition of entropy in the micro-canonical ensemble is

$$S = k_B \ln \Omega_s(N,V,E), \tag{2.7}$$

where $k_B = 1.381 \cdot 10^{-23}$ J/K is Boltzmann's constant. In terms of the level density $\rho(E)$, we have

$$S = k_B \ln \frac{\rho(E)}{\rho_0} = k_B \ln \rho(E) + S_0, \tag{2.8}$$

where we have inserted Eq. (2.6), divided by a normalization constant ρ_0, into Eq. (2.7). The constant S_0 is determined by applying the third law of thermodynamics which states that when the temperature goes to zero, the entropy will also tend to go to zero or to a constant value. Further we can find the temperature for a system in equilibrium through the relation

$$T = \left(\frac{\delta S}{\delta E} \right)^{-1}_V. \tag{2.9}$$

Obviously the constant S_0 will not survive the derivation, and does thereby not influence the temperature. However, slight changes in $\ln \rho(E)$ can cause significant changes in the temperature. It is these changes that can cause negative values of the temperature, as a result of the derivation.
Another important quantity that characterizes a system is its heat capacity C_V. The heat capacity gives a measure of how fast the temperature increase with increasing energy, and is in the micro-canonical ensemble expressed by

$$C_V = \left(\frac{\delta T}{\delta E} \right)_V. \tag{2.10}$$

Because negative slopes can occur in the temperature as a function of excitation energy, this will create negative values of the heat capacity.

2.2.2 The canonical ensemble

Because of the limitations described for the micro-canonical ensemble, we will also present results derived from the canonical ensemble, where the system is brought into thermal contact with a reservoir with constant temperature. However, this ensemble is probably not ideal. In the canonical ensemble the energy E can fluctuate while the size of the system V is assumed to be fixed.

The partition function in the canonical ensemble $Z(T)$ is expressed as the Laplace transformation of the multiplicity of states $\omega(E_i)$

$$Z(T) = \sum_{i=0}^{\infty} \omega(E_i) e^{-E_i/k_B T}, \tag{2.11}$$

where $\omega(E_i) = \delta E_i \rho(E_i)$, where E_i is the excitation energy, δE_i is a small energy interval and $\rho(E_i)$ is the level density at excitation energy E_i. The Boltzmann's constant is given by k_B and the temperature is represented by the factor T. As a result of the summation structural changes will be smoothed as a function of excitation energy. From the partition function we can derive all other thermodynamic quantities. As a starting point let us look at the Helmholtz free energy F, defined by

$$F(T) = -k_B T \ln Z(T). \tag{2.12}$$

This can also be expressed through the partition function

$$F = \langle E \rangle - TS. \tag{2.13}$$

Taking the differential of Eq. (2.12) and using the *thermodynamic identity*

$$d\langle E \rangle = TdS - pdV, \tag{2.14}$$

where p represents the pressure, we find that the entropy can be written as

$$S(T) = -\left(\frac{\delta F}{\delta T}\right)_V, \tag{2.15}$$

for a constant volume V. The average energy $\langle E \rangle$ in the canonical ensemble can be expressed as follows

$$\langle E \rangle = -T^2 \left(\frac{\delta(F/T)}{T}\right)_V. \tag{2.16}$$

Further the canonical heat capacity is defined as the derivative of the energy E with respect to the temperature

$$C_V = \left(\frac{\delta \langle E \rangle}{\delta T}\right)_V. \tag{2.17}$$

2.3 The γ-ray strength function

The γ-ray strength function is a measure of the average electromagnetic properties of the nucleus. Through emission of electromagnetic radiation the nucleus can change its electromagnetic moment. By emission of γ rays the angular momentum can change with one or several units. The total angular momentum must be conserved and the γ-ray will carry the angular momentum *lost* by the nucleus, equal to $L\hbar$ where L is the quantum number for angular momentum. The numbers that L can attain must be integers above zero, $L = 1, 2, ...; L \neq 0$, where $L = 1$ characterizes a dipole, $L = 2$ a quadrupole, $L = 3$ a octupole etc. Further the parity of the radiation distinguishes between electric and magnetic multipole radiation. Electric multipole radiation have even parity if L is even, while magnetic multipole radiation have even parity if L is odd.

The total γ-ray strength function consists of the sum over all strengths of all possible polarities. The probability of the different multipole radiation decreases drastically with increasing angular momentum L. In general, photon emission with a multipolarity $L+1$ is less probable than the photon emission with a multipolarity L by a factor of 10^{-6}. For this reason the dipole radiation will dominate the strength function. Further the probability for emission of electric multipole radiation is an order of two larger than the probability of emission of magnetic multipole radiation.

Bartholomew [15] described in 1972 the strength function f_{XL}, for a transition of multipolarity L and electric or magnetic type X from an initial state i to a final state f through the expression;

$$f_{XL} = \frac{\langle \Gamma_{\gamma if} \rangle}{E_\gamma^{2L+1} D_i}, \tag{2.18}$$

where $\langle \Gamma_{\gamma if} \rangle$ is the radiative width, D_i is the level spacing of the initial states and E_γ gives the transition energy.

2.3.1 Pygmy resonance

The pygmy resonance is a common name describing non statistical features in quasi-continuous γ-ray spectra observed at energies below the giant electric dipole resonance (GEDR). The GEDR will be discussed in the next section. In the rare earth isotopes a pygmy resonance is observed at approximately 3 MeV. This gives rise to a little bump in the γ-ray strength function, centered at about 3 MeV. One usually parametrizes the 3 MeV pygmy resonance by a Lorentzian function $f_{py}(E_\gamma)$ [16]

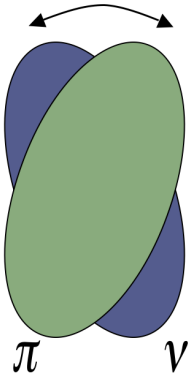

Figure 2.1: *The scissor mode where protons are clipping against neutrons in the nucleus.*

$$f_{py}(E_\gamma) = \sigma_{py}\left(1+\frac{(E_\gamma^2-E_{py}^2)^2}{E_\gamma^2\Gamma_{py^2}}\right)^{-1}, \tag{2.19}$$

where σ_{py}, E_{py} and Γ_{py} represent the strength, centroid and width of the pygmy resonance, respectively. The parameter E_γ gives the γ-ray energy. All these parameters are obtained by fit to experimental data, details of this fitting procedure is outlined in chapter 6.

The Oslo group has investigated the probability that the 3 MeV pygmy resonance in rare earth isotopes is due to the so called scissor mode. In Ref. [2] the M1 multipolarity of the pygmy resonance was established. The name scissor mode originate from the geometrical interpretation of the mode as a scissor like motion where the protons are clipping against the neutrons, see Fig. 2.1.

2.3.2 Giant electric and magnetic dipole resonance

At γ-ray energies around $12-14$ MeV, in medium heavy and heavy nuclei, the giant electric dipole resonance (GEDR) is observed. Geometrically it is interpreted to originate from oscillation of protons against neutrons in the nucleus, as illustrated in Fig. 2.2. The Brink-Axel hypothesis [17, 18] states that collective excitations built on excited states have the same properties as those built on the ground state. As a consequence the γ-decay is only dependent on γ-ray energy E_γ, not on the temperature of the final state. As a result the GEDR has a Lorentzian shape [19]

$$f_{E1}(E_\gamma) = \frac{1}{3\pi^2\hbar^2c^2}\frac{\sigma_{E1}\Gamma_{E1}^2E_\gamma}{(E_\gamma^2-E_{E1}^2)^2+\Gamma_{E1}^2E_\gamma^2}, \tag{2.20}$$

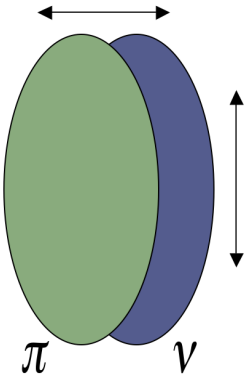

Figure 2.2: *The giant electric dipole resonance where the protons and neutrons are oscillating against each other.*

where σ_{E1}, Γ_{E1} and E_{E1} represents the strength, width and centroid energy of the GEDR, respectively. This expression provides a very good description of the GEDR close to the centroid, for medium heavy and heavy nuclei. However, in the low excitation energy region the γ-ray strength predicted from Eq. (2.20) is less than the observed value. In the present work we will apply a method developed by Kadmenskiĭ, Markushev and Furman (KMF model) [20]. In this model there is a temperature dependence on the final states T_f,

$$f_{E1}^{KMF}(E_\gamma) = \frac{1}{3\pi^2\hbar^2c^2}\frac{0.7\sigma_{E1}E_\gamma\Gamma_{E1}^2(E_\gamma^2+4\pi^2T_f^2)}{E_{E1}(E_\gamma^2-E_{E1}^2)^2}, \tag{2.21}$$

The KMF model describes the low energy region we are interested in very good. However, the temperature dependence contradicts the Brink-Axel hypothesis. The KMF model fails to describe the GEDR close to the centroid, where Eq. (2.21) diverges.

As illustrated by the horizontal and vertical arrows in Fig. 2.2, there are two different axes, in deformed nuclei, where the protons and neutron can oscillate against each other. This results in a splitting of the GEDR that can be parametrized by two functions given by either Eq. (2.20) or Eq. (2.21), depending on the energy region under consideration.

In the γ-ray strength function one also observes a giant magnetic dipole resonance (GMDR). This is believed to be governed by the spin-flip M1 resonance [21]. It is described by the following function [4]

$$f_{M1}(E_\gamma) = \frac{1}{3\pi^2\hbar^2c^2}\frac{\sigma_{M1}E_\gamma\Gamma_{M1}^2}{(E_\gamma^2-E_{M1}^2)^2+E_\gamma^2\Gamma_{M1}^2}, \tag{2.22}$$

where σ_{M1}, Γ_{M1} and E_{M1} represents the strength, width and centroid of the resonance, respectively. The expressions both for the GEDR and GMDR along with the expression for the pygmy resonance will be taken in use in chapter 6, where the predicted total γ-ray strength function is fitted to the experimental data.

Chapter 3

Experimental method and data analysis

The experiment was performed at the Oslo Cyclotron Laboratory (OCL) in June 2006. It was a very successful run, with more than 15 Gb of data collected over a running time of 11 days. In the following sections an outline will be given on how the data was handled and saved, and the data analysis will be described.

3.1 Experimental details and detector setup

The accelerator at the OCL is a Scanditronix MC-35 cyclotron. It was used to accelerate a beam of ^{3}He particles to an energy of 38 MeV. As a target we used a 1.73 mg/cm^2 thick foil of 98.5 % enriched ^{164}Dy. The excited ^{163}Dy was produced through the pick up reaction; ^{164}Dy(^{3}He,α)^{163}Dy, whereas ^{164}Dy was excited through inelastic scattering from the Coulomb interaction between the projectile and the target; ^{164}Dy(^{3}He,^{3}He$'$)^{164}Dy. The corresponding Q-values[1] are 12.92 MeV and 0 MeV, respectively. The ejectiles and the γ rays were detected with the CACTUS multi-detector array [22], that consists of 28 NaI(Tl) γ detectors and eight particle telescopes made of silicon. The detector configuration is illustrated schematically in Fig. 3.1. The NaI(Tl) detectors in the array are mounted in a spherical frame with a radius of 250 mm. The distance between the target position and the γ-detectors are 220 mm. All the NaI detectors are equipped with a lead collimator which has an inner diameter of 7 cm and a thickness of 10 cm. In front of the detectors a 2 mm Cu absorber is placed to shield against low energy x-ray radiation. The total efficiency of the NaI(Tl) detectors is measured to be 15% of 4π. The NaI(Tl) detectors has an energy resolution of 8 keV determined from the full width at half maximum (FWHM) at an energy of 1.33 MeV. These are

[1] The Q-value denotes the amount of energy released in the reaction.

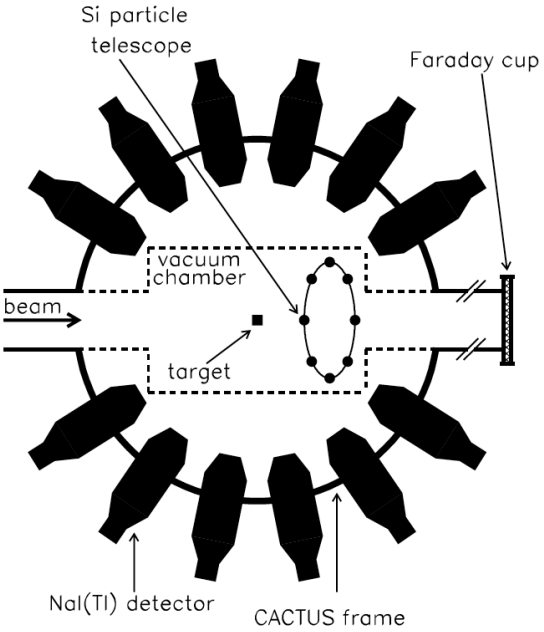

Figure 3.1: *Schematic drawing of the CACTUS multidetector array, taken from Ref. [23].*

suitable detectors for our type of experiments due to their high efficiency, which remains almost constant and independent of γ-ray energy. The particle telescopes are placed in a vacuum chamber inside the detector frame located at the end of the beam tube. The vacuum ensures that the particles are not scattered or lose energy before reaching the telescopes. Each telescope makes an angle of 45° relative to the incoming beam, in a forward direction with respect to the beam axis. The Si detectors are placed approximately 5 cm from the target. The telescopes consist of a front detector that slows the particles down and an end detector where the particles stops. Particles that arrive in a narrow angle with respect to the telescope axis might escape the detectors without depositing their full energy. In order to stop such particles a 6 mm thick Al collimator with a diameter of 5 mm is placed in front of each telescope. In addition, a 19 μm thick Al foil is placed in front of each collimator in order to absorb low energy δ electrons[2]. Our experimental energy resolution of the elastic ^{3}He peak is measured to be 260 keV. The particle telescopes have a total solid angle coverage of around 0.7 % of 4π.

A Faraday cup is located at a distance of 1.5 m outside the detector frame to stop the incident beam.

[2]The δ electrons are atomic electrons released from the target after Coulomb interaction with the projectile.

3.2 Signal treatment

When a particle hits a Si telescope an electric signal is generated. The signal is amplified and sent through the electronics setup. A crucial part of this setup is to measure particle-γ coincidences. The particle type detected by the Si telescopes give information of which excited ^{163}Dy or ^{164}Dy nucleus that has been created. The γ-rays detected simultaneously with this particle will then origin from this nucleus. We therefore want to measure which γ-rays are detected simultaneously with the various particles. The coincidence unit generates a signal if all the three following criteria are met

(i) Only one front detector is hit.

(ii) The particle front detector signal is higher than a threshold set to $Z > 1$, for the constant fraction discriminator (CFD).

(iii) At least one particle end detector is hit.

There is no requirement that the particle front and end detector that register a hit belong to the same telescope. However, this is not a considerable problem because the particle multiplicity and the beam current are relatively low. The second criteria rules out the electrons and hydrogen isotopes. The particle-γ coincidences are tested by a veto discriminator. If it registers a coincidence a logic signal is generated to start a time-to-digital converter (TDC)[3]. Then a delayed signal from a CFD, which is connected to the NaI which detected a γ-ray, is used to stop the TDC. The time interval measured in between the start and stop pulses is digitized and contains the time information for an event.

3.3 Particle identification

To be able to distinguish which γ-rays that belong to which reaction, we have to identify the various projectiles produced. Each particle telescope has a thin front detector where the particles deposit some energy ΔE and a thick end detector where the particles are stopped and thereby deposit the rest of the energy E. The various particles will lose energy mainly due to ionization. How different particles deposit energy in a medium is described through the Bethe-Block formula [24]:

$$-\frac{dE}{dx} = 2\pi N_a r_e^2 m_e c^2 \rho \frac{Z}{A}\frac{z^2}{\beta^2}\left[\ln\left(\frac{2m_e\gamma^2 v^2 W_{max}}{I^2}\right) - 2\beta^2\right], \tag{3.1}$$

[3] A TAC and a ADC connected together

where N_a is Avagadros number ($6.022 \cdot 10^{23}$ mol^{-1}), r_e is the classical electron radius ($2.817 \cdot 10^{13}$ cm) and m_e is the mass of the electron, z is the charge of the incoming particle, Z, A and ρ are the atom number, mass number and the density, respectively, of the absorbing material. The factor β is given by, $\beta = v/c$, where v is the speed of the particle and c is the speed of light. The factor γ is given by $\gamma = 1/\sqrt{1-\beta^2}$. The mean excitation potential is denoted by I, while the maximum energy transferred in a single collision is given by W_{max}.

For the same type of particles, the amount of energy deposited in the front and end detectors varies with the energy of the particles. From Eq. (3.1) it follows that the energy deposition increases when a charged particle is slowed down. In addition the mass and charge of a particle will also influence the energy deposition. When plotting the energy deposition in the front detector versus the energy deposition in the end detector, a unique banana-shaped curve is found for each particle type. Such a plot is given in Fig. 3.2, where the uppermost curve represents the α particles. The curve below this is the ^{3}He curve, where we observe a peak located at approximately 32 MeV in the end detector. This peak corresponds to the elastic ^{3}He peak. Diagonal to this peak we observe a *tail*, which is most likely due to a small amount of ejectiles channeling through the polycrystalline structure of the front detector. As a result too little energy is deposited in the front detector. The sharp vertical line seen in the spectrum above the elastic peak corresponds to the case when δ-electrons deposit energy in the front detector along with elastically scattered ^{3}He-particles. Below the elastic peak there is another vertical line that originates when some of the energy deposited in the front detector is not collected. Similarly the horizontal line to the left of the peak is due to failure in collecting all the energy in the end detector. At the bottom left of Fig. 3.2, curves corresponding to tritons, deuterons and protons are observed.

From these banana-shaped curves we are able to calculate the range $R(E)$ of the particles of interest. The range of a particle describes how far the particle can penetrate in a certain medium as a function of energy. Experiments performed with the CACTUS multi-detector array showed that the range curve can be described accurately with the following parameterization [25]

$$R(E) = aE^{(b+c)\log E}, \tag{3.2}$$

where a, b and c are free parameters, and E gives the kinetic energy of the particle. From this we can derive a *thickness* spectrum that gives the thickness of the front detector as a function of particle type. This is obtained by subtracting the range for the particle in the end detector from the total range of the particle.

$$R(\Delta E + E) - R(E) = d_{\text{front}} \tag{3.3}$$

Here, ΔE and E give the energy deposited in the front and end detector, re-

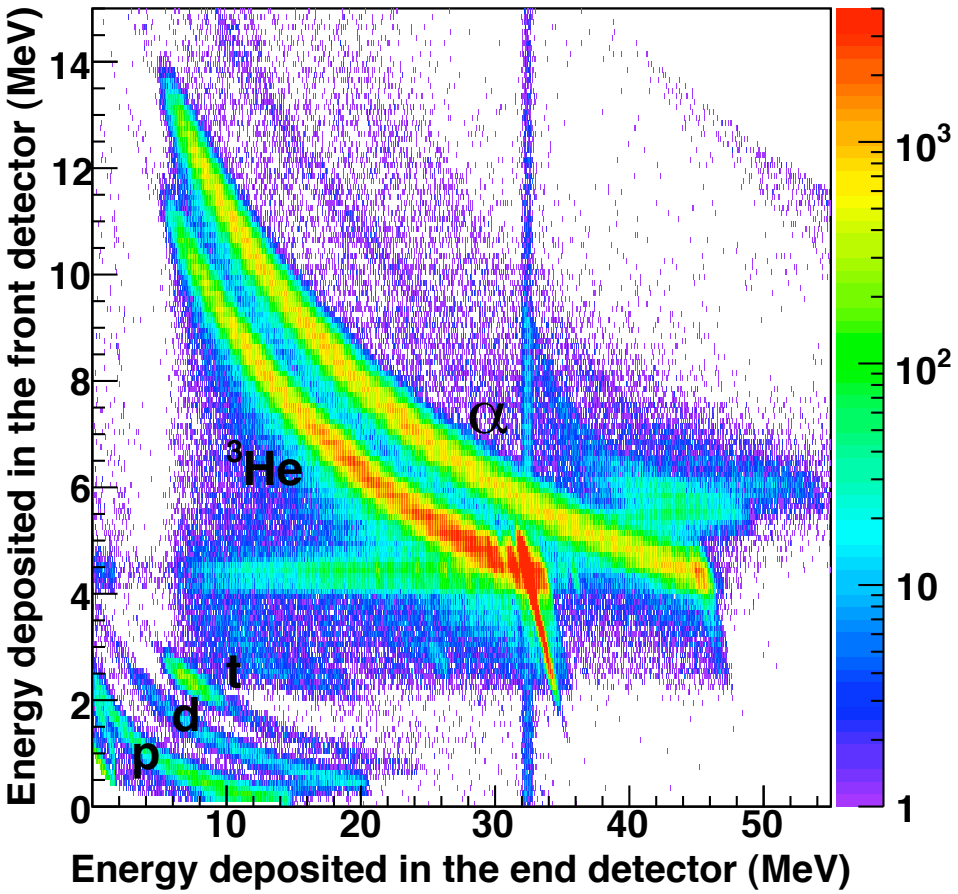

Figure 3.2: *Energy deposited in the front detector versus energy deposited in the end detector, see explanation in the text of Sec.* 3.3.

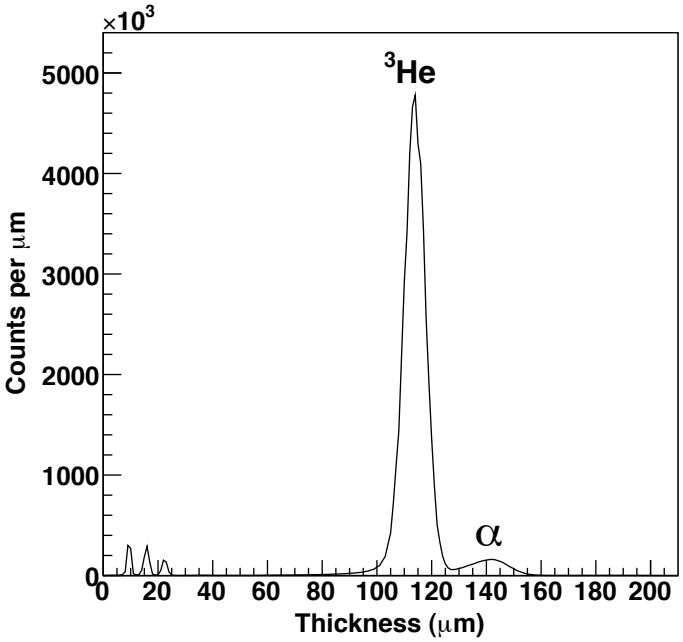

Figure 3.3: *Thickness spectrum of particle telescope 6. This spectrum is used to set gates on the* ^{3}He *and* α *particles*

spectively. The free parameters of Eq. (3.2) are determined by using the banana shaped curves in Fig. 3.2 along with Eq. (3.3). In software the data are sorted with a range curve, for example for the α particles, to obtain a thickness spectrum. Such a spectrum is shown in Fig. 3.3. The α peak in Fig. 3.3 corresponds to the front detector's true thickness. By looking at the thickness spectrum we are able to set gates for the ^{3}He and α particles which are used in subsequent data sorting routines to extract the $\alpha - \gamma$ and ^{3}He-γ coincidences.

3.4 The time spectrum

A TDC (one for each NaI(Tl)) records the time interval between the input start and stop pulses arriving. A start signal is created when a charged particle is detected in a Si telescope, and a stop signal is created when γ-rays are registered in the NaI(Tl) detectors. If the interval between the start and stop pulses are less than a time window set to 410 ns, the time signals are stored. However, a delay of a ≈ 250 ns is put on the stop signal, in this way we will register events where the γ-rays in real time are detected before the particle. The distribution of these digitized

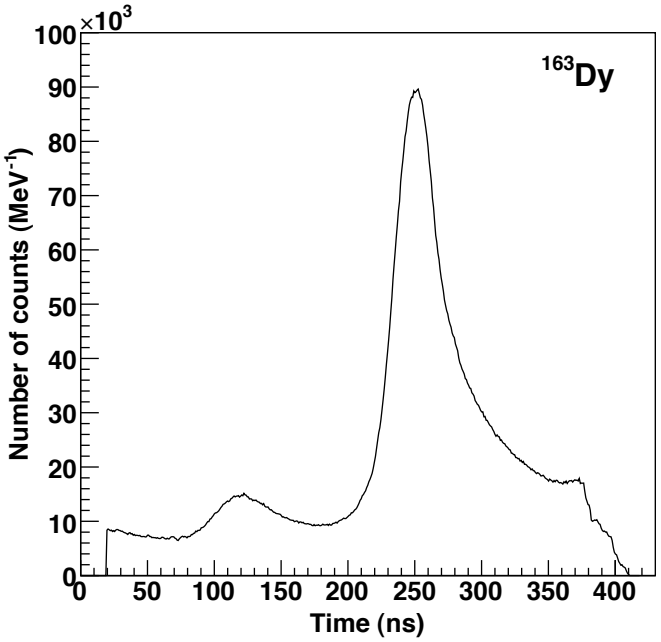

Figure 3.4: *The time spectrum, where an α-particle gives the start signal. The largest peak corresponds to true coincidences.*

time signals are called the time spectrum, see Fig. 3.4. This time spectrum is used to determine whether the γ-rays detected are in coincidence with a particle, and hence origin from the same nuclear reaction. We observe in Fig. 3.4 that the position of the largest peak is centered around 250 ns. This corresponds to the true coincident events, due to the delay of the stop signal this is located at 250 ns instead of 0 ns.

The particles in the beam arrive at the target in *bunches* with a period of 130 ns. Because our time window is larger than the beam period, we will detect events that do not originate from the same beam pulse. This explains the smaller peak on the left side of the coincidence peak. Also on the right side of the beginning of a small peak is shown, see Fig. 3.4. In the right peak the particle is measured in coincidence with a γ-ray from the next beam pulse, and in the left peak the γ-ray stems from a reaction induced by the previous beam pulse. In addition, there is a steady number of random coincidences caused by background radiation.

We now want to extract the true coincidences from the data. This is done by setting a window on the true coincidence peak and one window on the left peak. Events that fall into the coincidence window are incremented, while events that fall into the random window are decremented. Everything else is rejected.

3.5 The particle spectra

Using the gates set in the thickness spectrum as described in Sec. 3.3 we are able to sort out the α and the ^{3}He particles from the data. The spectrum obtained is called a singles spectrum and contains the total number of the particles of interest as a function of the particle energy. Further, using the windows set in the time spectrum, we can separate which particles are in coincidence with one or more γ-rays.

In Figs. 3.5 and 3.6 the α and ^{3}He coincidence spectrums are displayed, respectively, and compared to the singles spectrum. In the singles spectrum for the α particles in Fig. 3.5, we observe a peak with an energy of 49.6 MeV. This peak corresponds to the maximum energy the α particle can obtain, $E_\alpha(\max)$. The energy of the α particle E_α plus the energy E transferred from this particle to excite the nucleus, remains equal when we neglect the small recoil energy of the target nucleus. This total energy E_{tot} corresponds to the maximum α energy,

$$E_{\text{tot}} = E + E_\alpha, \tag{3.4}$$

where $E_{\text{tot}} = E_\alpha(\max)$. Further, this peak gives the population of the ground state, hence one cannot measure α particles of this energy in coincidence with γ-rays. Therefore, the $E_\alpha(\max)$ peak is not seen in the coincidence spectrum. One can also note a decrease in counts in the coincidence spectrum around 43.3 MeV. The energy transferred from the α particle to the nucleus in this case, $E_{\text{tot}} - E_\alpha = (49.6 - 43.3)\text{MeV} = 6.3$ MeV, equals the neutron binding energy in ^{163}Dy. Therefore, the γ decay in this region will compete with neutron emission. A similar decrease in counts is observed in the ^{3}He coincidence spectrum around 29 MeV, which corresponds to an energy transferred to the nucleus equal to the binding energy of the neutron in ^{164}Dy, namely 7.7 MeV. In the singles spectrum for this particle we observe a large peak located at 36.8 MeV, which is due to the elastic scattering of ^{3}He particles on the target nucleus. This type of scattering will populate the ground state in ^{164}Dy, and we will therefore not observe this peak in the coincidence spectrum. We observe pronounced peaks in both particle coincidence spectra, however we cannot be certain of which levels that built up these peaks. The reason for this is that information about discrete levels of ^{163,164}Dy found through the reactions ^{164}Dy(^{3}He, α)^{163}Dy and ^{164}Dy(^{3}He,^{3}He$'$)^{164}Dy, can not be found in literature.

When studying the coincidence spectra in Figs. 3.5 and 3.6 we observe data registered below the neutron binding energy. This is caused by other reaction channels, namely ^{164}Dy(^{3}He, αxn) and ^{164}Dy(^{3}He,^{3}Hexn), where the emission of α and ^{3}He particles are accompanied by a certain number of neutrons x. The more particles emitted, the more particles have to share the energy given by the projectile, thereby we observe the α and ^{3}He particles that originate from these

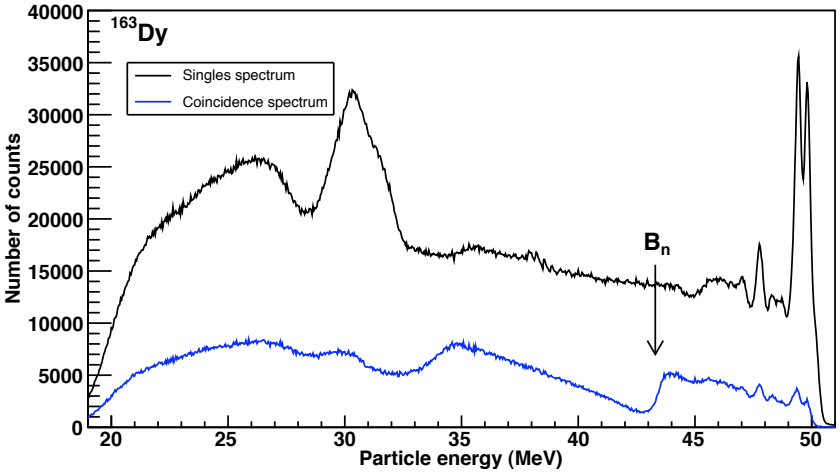

Figure 3.5: *The black spectrum gives the total number of counts for α particles as a function of energy. The blue spectrum is the number of α particles measured in coincidence with γ-rays as function of energy.*

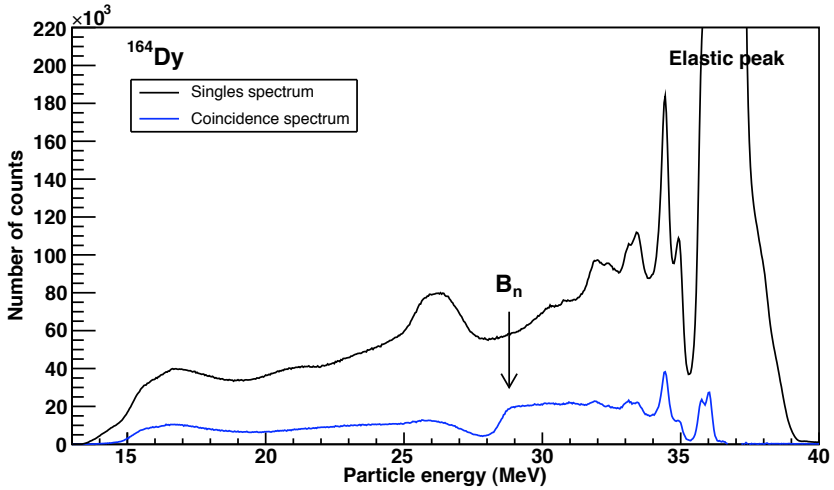

Figure 3.6: *The black spectrum gives the total number of counts for* ^{3}He *particles as a function of energy. The blue spectrum is the number of* ^{3}He *particles measured in coincidence with γ-rays as function of energy.*

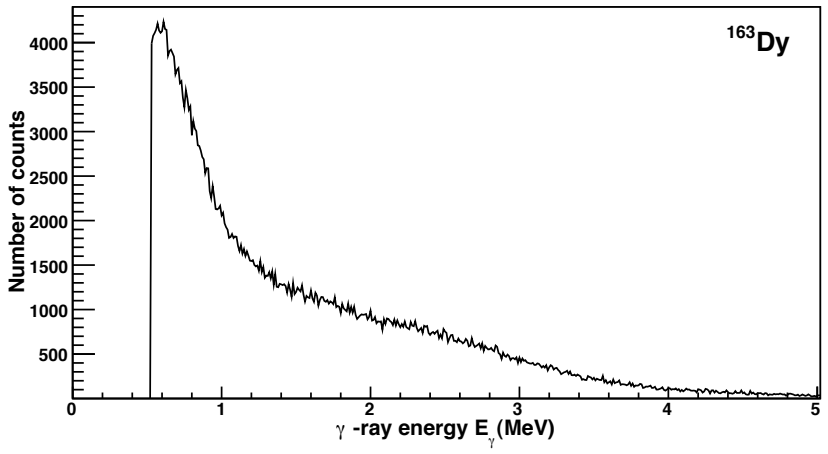

Figure 3.7: *The γ spectrum in coincidence with α particles, see explanation in the text of Sec. 3.6 and 3.7.*

reaction channels at a lower energy. In the further analysis we will only work with the region of the coincidence spectra that correspond to the $(^3\mathrm{He}, \alpha)$ and $(^3\mathrm{He},^3\mathrm{He}')$ reaction.

3.6 The γ spectra

Analogous to the particle spectra described in the previous section, we extract which γ-rays that came in coincidence with the α and ^{3}He particles. The CACTUS detector array enables us to study the γ-spectra obtained for different excitation energies in the nucleus. Gamma spectra obtained in the excitation region spanning from the ground state up to the neutron binding energy are displayed in Figs. 3.7 and 3.8 for α and ^{3}He coincidences, respectively. Due to a substantial amount of noise in the NaI electronics at low energies we do not have a reliable spectrum for energies below ~ 0.5 MeV. However, as will be explained in the next chapter, this will not complicate the rest of the analysis.

3.7 Unfolding the γ-ray spectra

The γ-rays emitted after a nuclear reaction are not measured directly, but instead interacts with the atomic electrons in the NaI(Tl) crystals, which we in turn are able to detect. The observed γ-spectrum displays a broad energy distribution with-

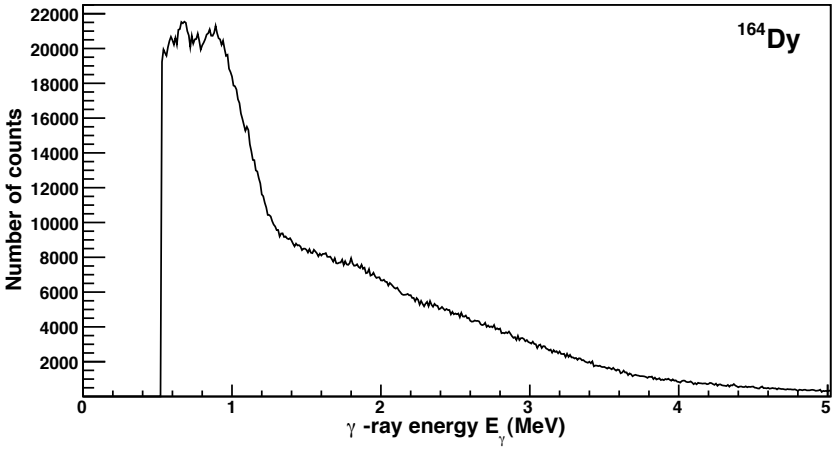

Figure 3.8: *The γ spectrum in coincidence with* ^{3}He *particles, see explanation in the text of Sec. 3.6 and 3.7.*

out sharp peaks, see Figs. 3.7 and 3.8. The spectrums are influenced by how the γ-rays interact with matter, and does not reflect the full energy of all the γ-rays. To retrieve the true energy of all the γ-rays an unfolding procedure is applied. This method will be outlined in the following.

3.7.1 The response function

The detector response function gives the response observed from a detector when it is exposed to monoenergetic radiation. The response function for the NaI detectors is determined by how the γ-rays interact with the NaI crystals. In addition, the design and geometry of the detector will play a role. Gamma rays interact with matter through the three following processes:

Photoelectric effect: The photon transfers all its energy to a bound electron. The electron is then released from the atom and will have almost the full energy of the incoming photon, except for the binding energy of the electron which is very small in comparison.

Compton scattering: The photon transfers only parts of its energy to the bound electron, which is released from the atom. The photon can be scattered in this way several times. Due to the finite size of the detector it is inevitable that some of these Compton scattered photons will escape the detector. This creates the so-called Compton continuum.

Pair production: Gamma rays with energies higher than 1022 keV may undergo pair production. In this process an electron e^- and a positron e^+ is created. The positron produced will annihilate with an atomic electron, and create two new γ-rays. If one of these annihilation photons escape the detector we will register the full energy of the incoming photon minus 511 keV, this peak is called the single-escape peak. If both photons leave the detector we get a peak 1022 keV to the left of the full energy peak, this is called the double-escape peak.

We are interested in the actual γ-ray energies emitted from the nucleus, and only in the full energy peak is the total energy preserved. We therefore need to know the response function of all the detectors for all γ-ray energies.

The response functions for the 28 NaI detectors in CACTUS were found by measuring the following ten monoenergetic γ-rays from known sources and in-beam experiments: 122, 245, 344, 662, 1173, 1333, 1836, 4439, 6130 og 15110 keV [26]. Further, we obtain the response functions for all γ-ray energies by interpolating between the known response functions. First the full energy peak and the single- and double escape peaks are removed, to simplify the interpolation of the Compton background and the prominent peaks. The interpolation of the prominent peaks are done by placing a Gaussian distribution at the interpolated peak positions with the proper intensity and energy width. Handling the Compton background is more complicated because the distribution is varying depending on the full energy, see Fig. 3.9.

The energy E transferred from a photon to an electron depends on the energy of the incoming photon

$$E = E_\gamma - \frac{E_\gamma}{1+\frac{E_\gamma}{m_e c^2}(1-\cos(\theta))}, \tag{3.5}$$

where θ is the scattering angle and E_γ is the γ-energy. The electron mass is given by m_e, and the speed of light is represented by c. The interpolation is performed between γ-energies that correspond to the same scattering angle. Since the energy of the electron depends strongly on E_γ and the scattering angle, this must be accounted for by normalizing the interpolated spectrum. The interpolated Compton background C between two known Compton backgrounds C_1 and C_2 is calculated from the following formula

$$C(E) = (\frac{dE}{d\theta})^{-1}_{E_\gamma}[C_1(E_1)(\frac{dE}{d\theta})_{E_{\gamma 1}} + \frac{E_\gamma - E_{\gamma 1}}{E_{\gamma 2} - E_{\gamma 1}}(C_2(E_2)(\frac{dE}{d\theta})_{E_{\gamma 2}} - C_1(E_1)(\frac{dE}{d\theta})_{E_{\gamma 1}})]. \tag{3.6}$$

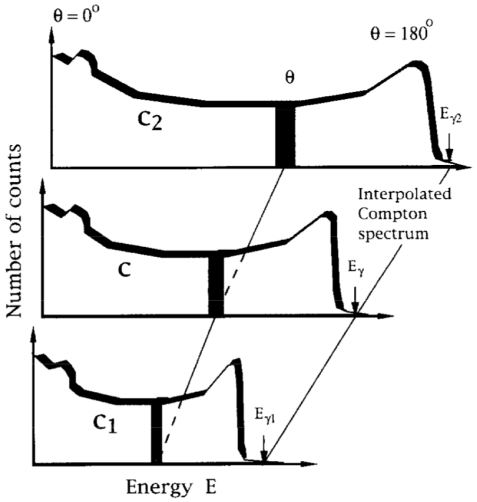

Figure 3.9: *Interpolation of the Compton part of the response functions C_1 and C_2, illustrating the increase of $\Delta\theta$ with the full energy E_γ. The figure is taken from Ref. [26].*

Here E_γ, $E_{\gamma 1}$ and $E_{\gamma 2}$ are the full energies for the interpolated spectrum and the reference spectra, respectively. The quantities E, E_1 and E_2 are the corresponding energies that the electron deposits in the detector due to Compton scattering into a angle θ. The terms $C(E)$, $C_1(E_1)$ and $C_2(E_2)$ represent the normalized number of counts for the corresponding energy deposited in each spectrum, see Fig. 3.9.

3.7.2 Folding iteration method

Through the folding iteration method we corrected for incomplete energy contributions from the total γ-ray spectrum, and a spectrum is created that contains the true energy of the incoming γ-rays. This spectrum is called an unfolded spectrum. The folding of a spectrum is described through the following expression [26],

$$\begin{pmatrix} f_1 \\ f_2 \\ \vdots \\ f_N \end{pmatrix} = \begin{pmatrix} R_{11} & R_{12} & \dots & R_{1N} \\ R_{21} & R_{22} & \dots & R_{2N} \\ \vdots & \vdots & \dots & \vdots \\ R_{N1} & R_{N2} & \dots & R_{NN} \end{pmatrix} \begin{pmatrix} u_1 \\ u_2 \\ \vdots \\ u_N \end{pmatrix}, \tag{3.7}$$

or in short form: $f = \mathbf{R}u$, where $\mathbf{R}$ is the response matrix , f and u are the folded and unfolded spectrum respectively. Through an iterative procedure where we start with a trial function u, which is folded and compared to the observed spec-

trum we obtain a better and better unfolded spectrum. This is performed through four steps [26]:

(1) Define a trial function u^0 equal to the observed spectrum r.

(2) Calculate the first folded spectrum by, $f^0 = \mathbf{R}u^0$.

(3) The next trial function is set equal the previous one plus the difference $r - f^0$,
$$u^1 = u^0 + (r - f^0).$$

(4) Fold once more and obtain a new f^1 that is used to obtain the next trial function,
$$u^2 = u^1 + (r - f^1).$$

These steps are repeated until $f^i \sim r$, where i denotes the number of iterations. If one were to calculate the unfolded spectrum through the exact matrix inversion, $u = \mathbf{R}^{-1}r$, one would obtain high oscillations from channel to channel. This is because even small variations in $\mathbf{R}$ causes significant variations in $\mathbf{R}^{-1}$. If we proceeded with higher iterations the unfolded spectrum would become more and more similar to the exact solution. We therefore terminate the iteration when the folded spectrum agrees with the observed spectrum within the experimental uncertainties. Usually this is obtained after about ten iterations, for nuclei similar to the ones studied here.

3.7.3 The Compton subtraction method

The Compton subtraction method produces a less fluctuating unfolded spectrum u_0. As a starting point the unfolded spectrum obtained from the folding iteration method is used. A Compton-like spectrum is extracted, which can be strongly smoothed, since it has no abrupt peak structures [26]. The Compton part together with the single-escape, double-escape and annihilation peaks are subtracted from the observed spectrum. The first step in the method is to define a spectrum equal to the observed spectrum minus the Compton contribution, given by

$$v(i) = p_f(i)u_0(i) + w(i), \tag{3.8}$$

where $p_f u_0$ is the contribution from the full energy peak u_f, and $w = u_s + u_d + u_a$ is the contribution due to single escape, double escape og annihilation processes, expressed as

$$u_s(i - i_{511}) = p_s(i)u_0(i) \tag{3.9}$$

$$u_d(i - i_{1022}) = p_d(i)u_0(i) \tag{3.10}$$

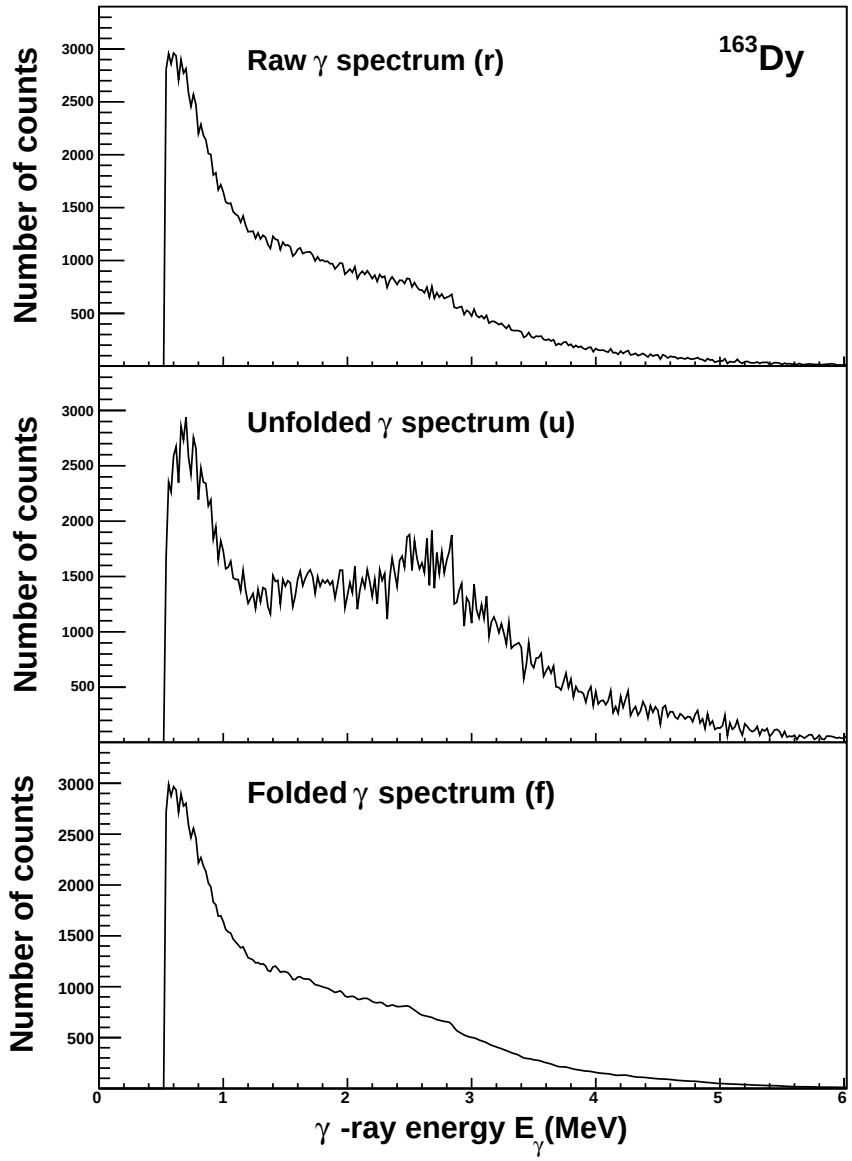

Figure 3.10: *The uppermost panel gives the observed raw γ-spectrum, while the middle panel is the unfolded spectrum, which after folding gives us the folded spectrum displayed in the lowest panel. All γ-ray spectrums are for the* ^{163}Dy *nucleus taken at excitation energy between* $4-6$ *MeV.*

$$u_a(i_{511}) = \sum_i p_a(i) u_0(i), \tag{3.11}$$

where i_{511} and i_{1022} correspond to the channels with the energies 511 and 1022 keV, respectively. The probabilities p_f, p_s, p_d and p_a are taken from Table 1 in Ref. [26]. The contributions in $v(i)$ have to be smoothed by an appropriate energy resolution. The spectra u_f, u_s and u_d have an energy resolution determined by both the experimentally observed spectrum (1.0 FWHM) and the response matrix (0.5 FWHM). Therefore the resolution is $\sqrt{1.0^2 + 0.5^2} = 0.87$. To obtain the experimental resolution, an additional smoothing of 0.5 FWHM is performed. The u_a spectrum will have all counts in channel i_{511} and must be smoothed with a resolution of 1.0 FWHM. Now we are able to determine the Compton background by

$$c(i) = r(i) - v(i) \tag{3.12}$$

This spectrum is smoothed with a additional 1.0 FWHM. Then the Compton term c and the peaks contained in the expression w are subtracted, and we correct for the full energy probability $p_f(i)$:

$$u(i) = [r(i) - c(i) - w(i)]/p_f(i). \tag{3.13}$$

Finally, we compute the true distribution of the γ-rays by correcting for the energy-dependent total γ detection efficiency ε_{tot},

$$U(i) = \frac{u(i)}{\varepsilon_{tot}(i)}. \tag{3.14}$$

The total γ-efficiency is given in ref. [26].

In Fig. 3.10 the result of this method is presented for the nucleus ^{163}Dy at excitation energy between $4-6$ MeV. The uppermost panel gives the observed raw γ-spectrum, while the lowest panel shows the folded spectrum. We observe that the folded spectrum shows a strong resemblance with the raw spectrum, this indicates that the method is reliable. The desired unfolded spectrum is displayed in the middle panel.

Chapter 4

The Oslo method

Both the level density and the γ-ray strength function can be extracted from one and the same experiment by use of the Oslo method. The starting point of the method is the first generation matrix, which will be obtained in the first section. The method is built upon the Brink-Axel hypothesis, which will be discussed in Sec. 4.2. In the following sections details on how the level density and the γ-ray strength function are derived from this hypothesis will be presented.

4.1 The first generation matrix

When an energy level below the neutron binding energy in an excited nucleus is populated, it will decay through a cascade of γ-rays. For the further analysis we want to extract the first γ-rays emitted in each such cascade. These γ-rays are used to construct the so-called first generation matrix, where the excitation energy is given versus the energy of the primary γ-rays. By normalizing the primary γ-ray spectrum to unity for each excitation energy, the first generation matrix will represent the decay probability for each γ-ray with energy E_γ decaying from a certain excitation energy E_i:

$$\sum_{E_\gamma=E_\gamma^{\min}}^{E_i} P(E_i,E_\gamma) = 1. \tag{4.1}$$

The first generation matrix is not straightforward to construct, because it cannot be experimentally resolved which γ-ray in a cascade that is emitted first. Since the detector registers all γ-rays in a cascade simultaneously, a subtraction method is developed to separate the primary γ-rays from the rest of the cascade [27]. An illustration of the method is given in Fig. 4.1. If we assume that an initial energy level E_i can decay by $\gamma_1,\gamma_2,\gamma_3,...,\gamma_j$, with decay probability $\omega_1^i,\omega_2^i,\omega_3^i,...,\omega_j^i$,

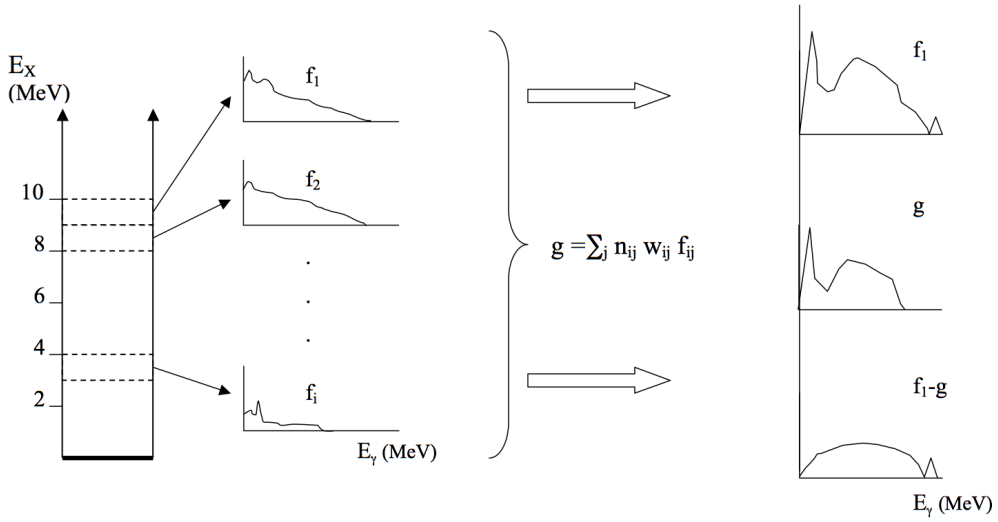

Figure 4.1: *Illustration of the method used to extract the primary γ-rays. Gamma-rays from different excitation energy regions are obtained by setting different gates in the unfolded particle-γ coincidence matrix. The illustration is based on Fig. 1 found in Ref. [30].*

one can obtain the first generation spectrum for the level E_i by subtracting the γ-ray spectra f_j that correspond to the energy levels E_j from the spectrum f_i. The subtraction can then be expressed as

$$h_i = f_i - g_i, \tag{4.2}$$

where

$$g_i = \sum_j n_j^i \omega_j^i f_j. \tag{4.3}$$

Here the coefficients ω_j^i represent the probability ($\sum \omega_i = 1$) of decay from bin i to bin j (each excitation energy bin is 120 keV wide). Because the different levels are populated with different probabilities, one must account for this when subtracting the weighted sum g_i from f_i. Therefore the coefficients n_i are determined such that the area of spectrum f_i multiplied by n_i corresponds to the same numbers of cascades. The particle singles cross section σ is proportional to the number of populated states and therefore also proportional to the number of cascades:

$$n_j^i = \frac{\sigma_i}{\sigma_j}, \tag{4.4}$$

Where σ_i and σ_j is the cross section measured for excitation region i and j, respectively. Further, we can calculate the average γ-ray multiplicity $\langle M \rangle$, which

is related to the γ-ray energy E_γ. We assume an N-fold population of an excited level E. The decay from this level will result in N γ-ray cascades, where the ith cascade contains M_i γ-rays. The average γ-ray energy $\langle E_\gamma \rangle$ is equal to the total energy carried by the γ-rays divided by the total number of γ-rays [32]:

$$\langle E_\gamma \rangle = N \cdot \frac{E}{\sum_{i=1}^{N} M_i} = \frac{E}{\frac{1}{N}\sum_{i=1}^{N} M_i} = \frac{E}{\langle M \rangle}. \tag{4.5}$$

From this we obtain the expression for the average multiplicity

$$\langle M \rangle = \frac{E}{\langle E_\gamma \rangle}. \tag{4.6}$$

The average γ-ray multiplicity $\langle M_i \rangle$ can thus be calculated for each excitation energy bin i. If $A(f_j)$ represents the number of counts (area) in the spectrum f_j, the cross section σ_j is proportional to $A(f_j)/\langle M_j \rangle$, and accordingly

$$n_j^i = \frac{A(f_i)/\langle M_i \rangle}{A(f_j)/\langle M_j \rangle} = \frac{A(f_i)\langle M_j \rangle}{A(f_j)\langle M_i \rangle}. \tag{4.7}$$

A small correction to Eq. (4.7) can be useful to introduce in order to compensate for an improper choice of weighing function ω_{ij}. We start by substituting g with αg, where α is close to unity. The area of the primary γ-ray spectrum is then

$$A(h) = A(f_i) - \alpha A(g), \tag{4.8}$$

which corresponds to a γ-ray multiplicity of one unit. Since the number of first generation γ-rays in the spectrum f_i equals $A(f_i)/\langle M_i \rangle$, $A(h_i)$ is also given by

$$A(h) = \frac{A(f_i)}{\langle M_i \rangle}. \tag{4.9}$$

Combining Eqs. (4.8) and (4.9) we obtain

$$\alpha = \left(1 - \frac{1}{\langle M_i \rangle}\right) \frac{A(f_i)}{A(g)}. \tag{4.10}$$

The parameter α can be varied in order to obtain the best agreement of the areas $A(h_i)$, $A(f_i)$ and $A(g_i)$. However, the correction should not exceed 15%, if a greater correction is necessary, then improved weighting functions ω_{ij} should be determined instead.

The weighting functions ω_j^i correspond to the first generation γ-spectrum h. This relationship is utilized when determining ω_j^i (and h) through a fast converging iterative procedure [27]. The method is composed of the following four steps:

(1) Apply a trial function ω_j^i.

(2) Calculate h_i.

(3) Transform h_i to ω_j^i, giving h_i the same energy calibration as ω_j^i and normalize the area of h_i to unity.

(4) If $\omega_j^i(\text{new}) \approx \omega_j^i(\text{old})$ finish the iterations, else proceed from step 2.

This method is based on some assumptions. The main assumption is that the γ-decay from a certain energy region is independent of the history of formation. This means that the levels populated by γ-decay from higher lying levels gives rise to exactly the same γ-emission pattern as the levels populated directly through the $(^3\text{He},^3\text{He}')$ or $(^3\text{He},\alpha)$ reactions, in the same energy region. This is fulfilled if the following two criteria are met

(i) The reaction $(^3\text{He},\alpha)$ or $(^3\text{He},^3\text{He}')$ populate approximately the same spin in each excitation interval.

(ii) About equally many states of positive and negative parity are populated in each excitation energy bin.

For each step in a γ-cascade the spin distribution becomes wider, however the average spin is approximately preserved when the cascade reaches the yrast line[1] [30]. Decay to the ground band is denoted as side feeding. From here the decay follows the ground band until the ground state is reached. One can hence obtain information about initial spin distribution by investigating the intensity of the side feeding to the ground band as a function of excitation energy [28, 29]. It was shown that the intensity of the side feeding to the ground state band transitions remains approximately the same over all excitation energies [30]. Therefore one can conclude that the spin population is approximately the same over the energy region under consideration [30].

Due to the dominance of E1 dipole transitions from the states populated in the quasi-continuum, there is a successive parity change in the cascade. As a result, γ-transitions subtracted from the γ-ray spectra in the subtraction method originate from states with opposite parity of those populated after emission of the first generation γ-rays [30]. If the population of both parities are equal, as is the case for low excitation energies [33], this would not be a problem. One can assume that this is correct for the whole energy range because the damping width[2]

[1]The yrast line refers to states of the nucleus which has the lowest excitation energy possible for a given angular momentum.

[2]The damping width is connected to the superposition of wave functions from neighboring levels [34].

is much larger than the average separation of single particle states, this results in an effective smearing of the single particle strengths [30].

At low excitation energy there exist strong single particle effects. As a result the γ-emission is not statistical in this region. In the next sections the γ-ray strength function and the level density will be extracted from the first generation matrix. When doing this we will exclude a region of low excitation energy due to the non-statistical decay. The limits used are equal to 2.01 MeV and 2.24 MeV in ^{163}Dy and ^{164}Dy, respectively. The first generation method has a weakness in that it can not completely exclude yrast transitions from the first generation matrix. This is due to that the spin population distribution between low and high excitation regions are not taken into consideration in the first generation method. In addition there are limitations in the electronics that make the low γ-ray energy region not reliable. For these reasons we will also exclude the region in the first generation matrix that corresponds to γ-energies below 1.0 MeV and 1.2 MeV in ^{163}Dy and ^{164}Dy, respectively. All the limits are indicated in the first generation matrices displayed in Figs. 4.2 and 4.3, for ^{163}Dy and ^{164}Dy, respectively.

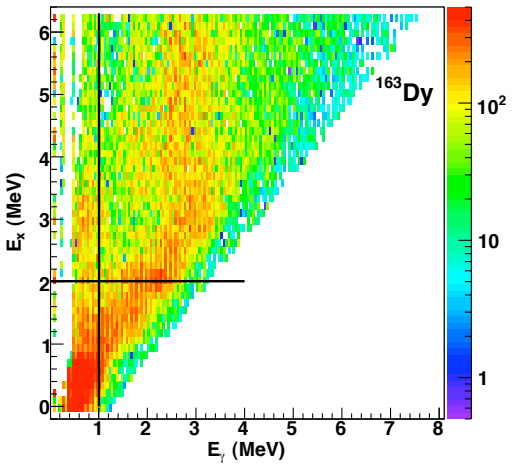

Figure 4.2: *The first generation matrix obtained for the ^{163}Dy nucleus. The solid lines in the spectrum gives the portion of the matrix which is used in the further analysis, see text of Sec. 4.1.*

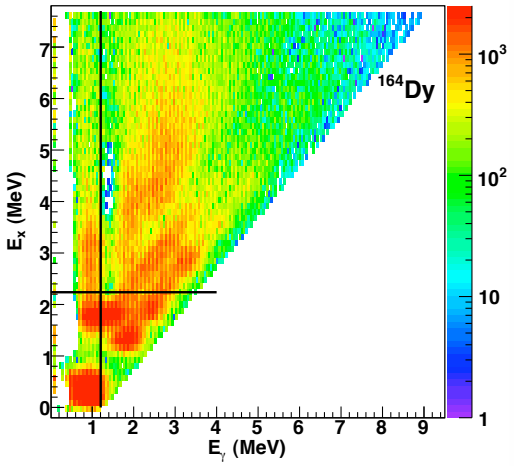

Figure 4.3: *The first generation matrix obtained for the ^{164}Dy nucleus. The solid lines in the spectrum gives the portion of the matrix which is used in the further analysis, see text of Sec. 4.1.*

4.2 The Brink-Axel hypothesis

The original Brink-Axel hypothesis [17, 18] states that the giant electric dipole resonance (GEDR) can be built on every excited state, and that the properties of the GEDR does not depend on the temperature of the nuclear state on which it is built [37]. This hypothesis can be generalized to include any type of collective excitation. This results in that the first generation matrix can be factorized as

$$P(E_i, E_\gamma) \propto \mathscr{T}(E_\gamma)\rho(E_i - E_\gamma), \tag{4.11}$$

where $P(E_i, E_\gamma)$ is the experimentally obtained and normalized first generation matrix. The final excitation energy E_f is given by the initial excitation energy minus the emitted γ-ray energy E_γ, as illustrated in Fig. 4.4. The decay probability of a γ-ray from an excited level E_i to a final level $E_f = E_i - E_\gamma$, is proportional to the product of the γ-transmission coefficient $\mathscr{T}(E_\gamma)$ and the level density at the final excitation energy $\rho(E_f)$. The above factorization is based on the essential assumption that the system is fully thermalized prior to γ-emission. The reaction can be described as a two-stage process of which the first is the formation of the compound nucleus, which subsequently decays in a manner that is independent of the mode of formation [31]. The formation of a complete compound state is as

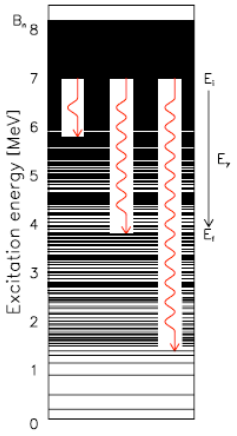

Figure 4.4: *The final energy level is give by the initial excitation energy minus the emitted γ-ray energy. The figure is taken from Ref. [1].*

fast as $\approx 10^{-18}$ s, significantly less than the typical life time of a state in the quasi-continuum which is $\approx 10^{-15}$ s. Thus, the nucleus "forgets" how it was formed and the decay process is statistical. Full thermalization is therefore expected to occur.

Experimentally it has been shown that the Brink-Axel hypothesis is invalid for high temperatures (above 1-2 MeV). Especially the width of the GEDR has shown to depend on the temperature of the final states [35]. Fermi-liquid models suggest a T^2 dependence for this effect [20, 36]. However, for the relatively low excitation energy range which is under study here ($T \leq 0.55$ MeV), the temperature dependence of the γ-transmission coefficient is not well known experimentally. The following assumptions are made [37]:

(i) The temperature varies little within the experimentally accessible excitation energy range (roughly $T \propto \sqrt{E}$).

(ii) The variations in the γ-transmission coefficient with temperature are small, roughly a second order effect in T [20].

Within these assumptions we can replace the temperature dependence of the transmission coefficient by a constant, average value $\langle T \rangle$ of the temperature. In this

way we recover the applicability of the generalized Brink-Axel hypothesis. The systematic error obtained by this approximation is largest for low energies (below 2-3 MeV) of the γ-ray transmission coefficient where it can reach $\sim 20\%$ [37].

Due to the normalizing condition given in Eq. (4.1), also the right hand side of Eq. (4.11) must be normalized to one at each excitation energy, this yields

$$P(E_i,E_\gamma) = \frac{\mathscr{T}(E_\gamma)\rho(E_i-E_\gamma)}{\sum_{E'_\gamma=E^{min}_\gamma}\mathscr{T}(E'_\gamma)\rho(E_i-E'_\gamma)}. \tag{4.12}$$

Using this equation and applying a least χ^2-fit to the primary γ-ray data we derive the functions ρ and $\mathscr{T}$ [1]. However, the level density and γ-transmission coefficient obtained from the χ^2 minimization is only one solution among an infinite number of solutions that reproduce the first generation matrix. All the solutions are related to each other through the two transformations [1]

$$\widetilde{\rho}(E_i-E_\gamma) = A\,\exp[\alpha(E_i-E_\gamma)]\,\rho(E_i-E_\gamma) \tag{4.13}$$

and

$$\widetilde{\mathscr{T}}(E_\gamma) = B\,\exp(\alpha E_\gamma)\,\mathscr{T}(E_\gamma), \tag{4.14}$$

where A, B and α are constants. These constants are determined by normalizing Eqs. (4.13) and (4.14) to known experimental data.

4.3 Normalizing the level density

The parameter α determines the slope of both the level density ρ and the γ-transmission coefficient $\mathscr{T}$, while the parameter A determines the magnitude of ρ. We therefore normalize Eq. (4.13) to known experimental data and thereby pick out the slope and magnitude which give us the most probable physical solution, from the infinite number of other options. At low excitation energy we assume that all levels are known. Information on discrete levels at low excitation energy are found in the database NNDC [38]. We normalize ρ to these known levels, the result can be viewed in Figs. 4.5 and 4.6 for ^{163}Dy and ^{164}Dy respectively, where the solid line represents the known levels and the dots are our experimental data points. The region between the arrows is used for the normalization.

The experimental level density is normalized to the level density determined from the known neutron resonance spacing data [19] at the neutron binding energy B_n. For the level density at B_n a Fermi gas model proposed by Gilbert and Cameron is used [7]:

$$\rho(U,J) = \frac{\sqrt{\pi}}{12}\frac{\exp(2\sqrt{aU})(2J+1)\exp\left[-(J+1/2)^2/2\sigma^2\right]}{2\sqrt{2\pi}\sigma^3} \tag{4.15}$$

$$\rho(U) = \frac{\sqrt{\pi}}{12}\frac{\exp(2\sqrt{aU})}{a^{1/4}U^{5/4}}\frac{1}{\sqrt{2\pi}\sigma}, \tag{4.16}$$

where $\rho(U,J)$ represents the level density for both parities for a given spin J, and $\rho(U)$ is the level density for all spins and parities. The parameter σ gives the spin dependence and a is the level density parameter. The intrinsic excitation energy is given by U. The neutron resonance spacing D for s-wave neutron capture[3] can be expressed as follows:

$$\frac{1}{D} = \frac{1}{2}\left[\rho(B_n, J = I+\frac{1}{2})) + \rho(B_n, J = I-\frac{1}{2}\right], \tag{4.17}$$

since all levels are accessible in neutron resonance experiments, and it is assumed that both parities contribute equally to the level density at the neutron binding energy B_n [1]. The spin of the target nucleus in a neutron resonance experiment is represented by I. When combining Eqs. (4.15)- (4.17) one can obtain an expression for the level density at the neutron binding energy given by

$$\rho(B_n) = \frac{2\sigma^2}{D}\frac{1}{(I+1)\exp(-(I+1)^2/2\sigma^2) + I\exp(-I^2/2\sigma^2)}, \tag{4.18}$$

where the spin-cutoff σ is calculated as follows [7]

$$\sigma^2 = 0.0888\sqrt{aU_n}A^{2/3}, \tag{4.19}$$

and A is the mass number of the nucleus. It is assumed that σ has an error of about 10% due to shell effects [7].

The extracted experimental level density cannot be compared directly to the calculated level density at the neutron binding energy, since the level density is only measured up to about $E = B_n - 1$ MeV. To reach the neutron binding energy we extrapolate the extracted experimental level density using the back-shifted Fermi gas level density [7, 8]:

$$\rho_{bs}(E) = \eta\frac{2\sqrt{a(U)}}{12\sqrt{2}a^{1/4}(U)^{5/4}\sigma}, \tag{4.20}$$

where η is a constant assigned to adjust ρ_{bs} to the experimental level density at B_n. The intrinsic excitation energy U is estimated by $U = E - C_1 - E_{\text{pair}}$, where C_1 is the back-shift parameter equal to $C_1 = -6.6A^{-0.32}$ MeV, and A is the mass number. The pairing energy E_{pair} is based on the pairing gap parameters Δ_p and Δ_n evaluated from odd-even mass differences [39] according to Ref. [40]. The spin-cutoff parameter σ is given by $\sigma^2 = 0.0888aTA^{2/3}$, where the nuclear temperature

[3] Absorption of a neutron followed by emission of γ-rays, (n,γ).

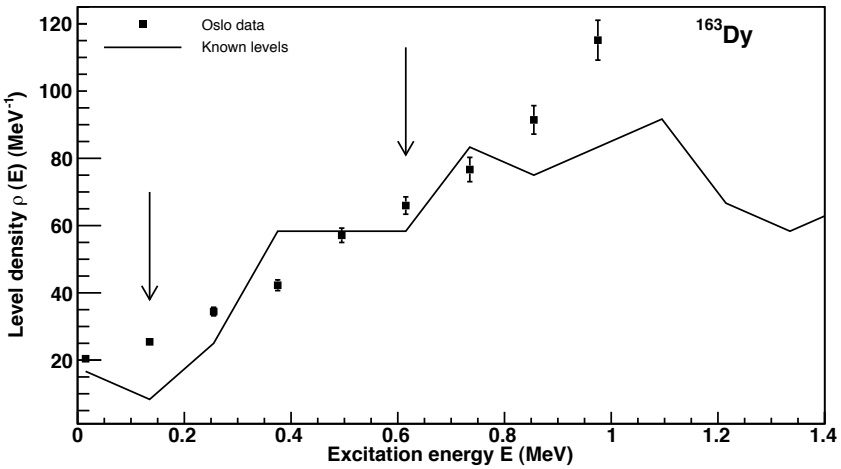

Figure 4.5: *Normalizing procedure of the level density of* ^{163}Dy *at low excitation energy. The data points between the arrows are adjusted to known levels.*

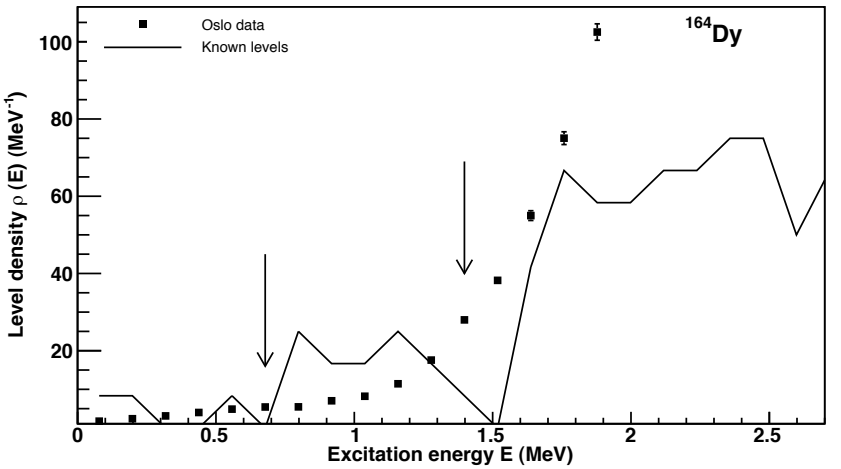

Figure 4.6: *Normalizing procedure of the level density of* ^{164}Dy *at low excitation energy. The data points between the arrows are adjusted to known levels.*

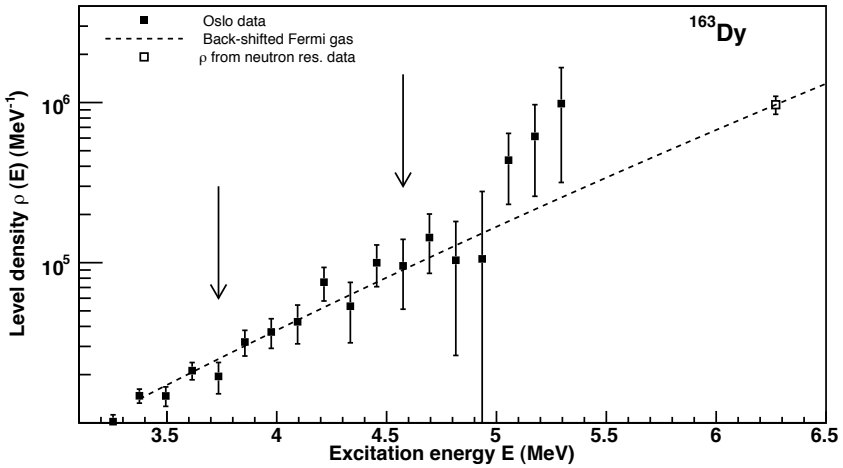

Figure 4.7: *Normalizing the level density of* ^{163}Dy *to the level density at the neutron binding energy by using an interpolation of the Fermi gas level density.*

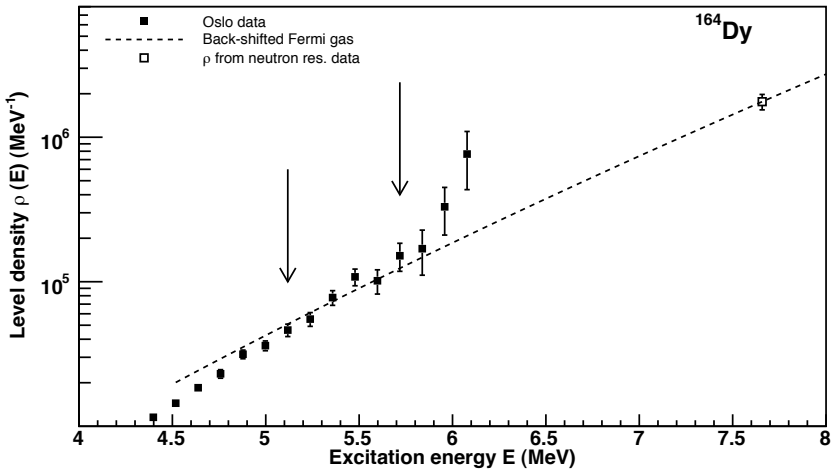

Figure 4.8: *Normalizing the level density of* ^{164}Dy *to the level density at the neutron binding energy by using an interpolation of the Fermi gas level density.*

Nucleus	E_{pair} (MeV)	a (MeV^{-1})	C_1 (MeV)	B_n (MeV)	D (eV)	$\rho(B_n)$ (10^6 MeV^{-1})	η
^{163}Dy	0	17.653	-1.293	6.271	62 (5)	0.969(125)	0.215
^{164}Dy	0.832	17.747	-1.291	7.658	6.8 (6)	1.762(215)	0.179

Table 4.1: *Parameters used for the level density with the back shifted Fermi gas model.*

is described by $T = \sqrt{U/a}$. In Figs. 4.7 and 4.8 the normalization of the level density according to the calculated value of $\rho(B_n)$ is displayed for ^{163}Dy and ^{164}Dy, respectively.

Recently, an improved method to calculate the level density at the neutron binding energy has been developed by Egidy and Bucurescu [9], as discussed in chapter 2. The spin-cutoff parameter of the new model is calculated from the expression [9]

$$\sigma^2 = 0.0146A^{5/3}\frac{1+\sqrt{1+4aU}}{2a}. \tag{4.21}$$

In addition, new improved measurements on the neutron resonance spacing have been accumulated. However, in the present analysis the method of Gilbert and Cameron is still employed. The reason for this is that results achieved from previous experiments on ^{160,161,162}Dy have been extracted by use of this model, comparing the results will thus be easier. When extracting the level density at the neutron binding energy from the model of Gilbert and Cameron we obtain values that are 34% and 32% lower than for what is achieved by the Egidy and Bucurescu model for ^{163}Dy and ^{164}Dy, respectively. In Table 4.1 follows a list of the parameters used for normalizing the level density.

It is important to note that the error bars displayed in all the figures only reflect the statistical uncertainties, and hence do not reflect the uncertainties related to the model used for normalization.

4.4 Normalizing the γ-transmission coefficient

All that is left to determine in order to normalize the γ-transmission coefficient is the constant B, which represents the magnitude of $\mathscr{T}$. The γ-transmission coefficients $\mathscr{T}$ for multipole type XL are related to the corresponding γ-strength functions by

$$\mathscr{T}_{XL}(E_\gamma) = 2\pi E_\gamma^{2L+1} f_{XL}(E_\gamma). \tag{4.22}$$

As described in chapter 2, the γ-decay taking place in the quasi-continuum is dominated by dipole transitions. Here one assumes that only such transitions give

a significant contribution to the γ-strength function. The observed $\mathscr{T}$ can then be described as a sum of only the $E1$ and $M1$ strength functions

$$B\mathscr{T}(E_\gamma) = B[\mathscr{T}_{E1}(E_\gamma) + \mathscr{T}_{M1}(E_\gamma)] = 2\pi E_{E_\gamma}^3[f_{E1}(E_\gamma) + f_{M1}(E_\gamma)]. \quad (4.23)$$

The parameter B represents the unknown normalization coefficient. In addition we assume that the number of positive and negative parity states are equal independent of energy and spin [21],

$$\rho(E_i - E_\gamma, I_f, \pm\Pi_f) = \frac{1}{2}\rho(E_i - E_\gamma, I_f). \quad (4.24)$$

The parameter B can be determined from the average total radiative width of compound states $\langle\Gamma_\gamma\rangle$. The experimental $\langle\Gamma_\gamma\rangle$ with excitation energy E, spin I and parity Π can be written in terms of the strength functions $f_{XL}(E_\gamma)$ [41]

$$\langle\Gamma_\gamma(E,I,\Pi)\rangle = \frac{1}{2\pi\rho(E,I,\Pi)}\sum_{XL}\sum_{I_f,\Pi_f}\int_0^E dE_\gamma \mathscr{T}(E_\gamma)\rho(E - E_\gamma, I_f, \Pi_f). \quad (4.25)$$

The summations run over all final levels with spin I_f and parity Π_f which are accessible by γ radiation with energy E_γ, and multipolarity XL. By combining Eqs. (4.23) and (4.24) in the expression (4.25), we can express the average total radiative width $\langle\Gamma_\gamma\rangle$ of neutron s-wave capture resonances with spin $I_t \pm \frac{1}{2}$ and excitation energy $E = B_n$

$$\begin{aligned}\langle\Gamma_\gamma(B_n, I_t \pm \frac{1}{2}, \Pi_t)\rangle &= \frac{1}{4\pi\rho(B_n, I_t \pm \frac{1}{2}, \Pi_t)}\int_0^{B_n} dE_\gamma B\mathscr{T}(E_\gamma)\rho(B_n - E_\gamma) \\ &\times \sum_{J=-1}^{1} g(B_n - E_\gamma, I_t \pm \frac{1}{2} + J), \end{aligned} \quad (4.26)$$

where I_t and Π_t denotes the spin and parity, respectively, of the target nucleus from the (n,γ)-reaction, and ρ is the experimentally obtained level density. Furthermore the level density is expressed as the product of the total level density and the sum of the spin distribution g given by [7]

$$g(E,I) = \frac{2I+1}{2\sigma^2}\exp\left[\frac{-(I+1/2)^2}{2\sigma^2}\right], \quad (4.27)$$

where σ is the same spin-cutoff parameter as the one used in Eq. (4.20). Further g is normalized so that $\sum_I g \approx 1$. The experimental width $\langle\Gamma_\gamma\rangle$ of Eq. (4.26)

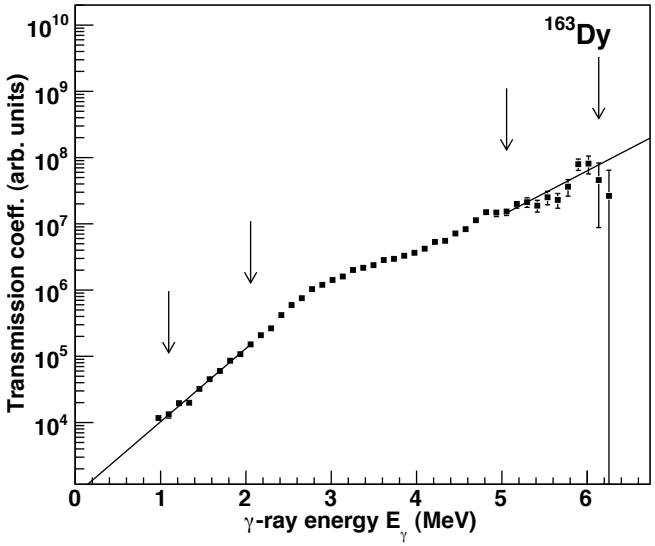

Figure 4.9: *Extrapolation of the γ transmission coefficient $\mathscr{T}$ in* ^{163}Dy. *The data points between the arrows are used for fitting the extrapolation.*

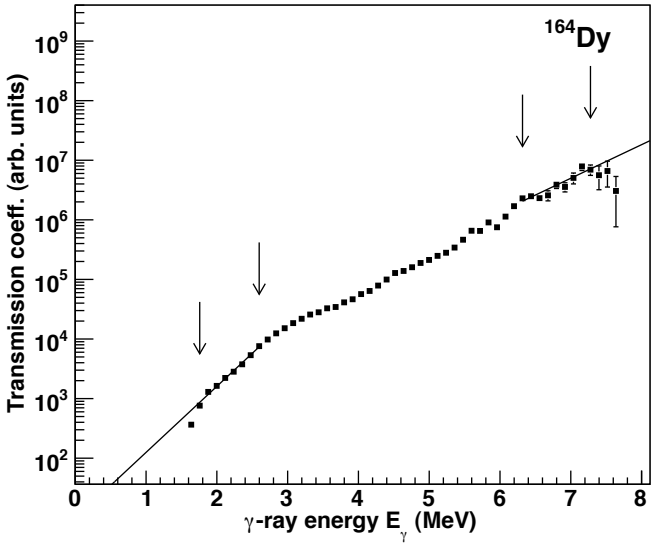

Figure 4.10: *Extrapolation of the γ transmission coefficient $\mathscr{T}$ in* ^{164}Dy. *The data points between the arrows are used for fitting the extrapolation.*

Nucleus	I_t	$\langle\Gamma_\gamma\rangle$ (meV)	B_n (MeV)	D	$\rho(B_n)$ (10^6 MeV^{-1})
^{163}Dy	0	112	6.271	62(5)	0.969(125)
^{164}Dy	$\frac{5}{2}$	113	7.658	6.8(6)	1.762(215)

Table 4.2: *Parameters used to normalize the γ-transmission coefficient.*

is then simply expressing the weighted sum of the contributions with spin $I_t \pm 1/2$.

As mentioned in the end of chapter 3, the region in the first generation matrix that corresponds to γ-ray energies below 1.0 MeV and 1.2 MeV for ^{163}Dy and ^{164}Dy, respectively, are not taken into consideration. In addition, the region that corresponds to γ-energies of $E_\gamma > B_n - 1$ MeV suffer from bad statistics. The γ-transmission coefficient $\mathscr{T}$ is therefore extrapolated in these regions using an exponential function. The data points between the arrows in Figs. 4.9 and 4.10 are used for fitting the extrapolation of ^{163}Dy and ^{164}Dy, respectively. The parameters used in the extrapolations are given in Table 4.2.

Chapter 5

Experimental level density and thermodynamic properties

In this chapter the final results extracted with the Oslo method will be presented. In the first section the level densities are shown, further we will look into thermodynamic properties derived from the level density. Results obtained from both the micro-canonical and the canonical ensemble are displayed.

5.1 The experimental level density

Rare earth isotopes are medium heavy well deformed nuclei. The fact that they are heavy and thus contain many nucleons means that there are many ways the nucleus can configure and therefore there are more degrees of freedom than for smaller systems. The nuclei ^{163,164}Dy exist in the mid-shell region, which makes a considerable amount of accessible states. The proton number of $Z = 66$ is right in between the closed shells of 50 and 82 protons. Also the neutron numbers of $N = 97$ and $N = 98$ for ^{163}Dy and ^{164}Dy, respectively, are far away from the closed shells at 82 and 126 neutrons. Thus we observe a high level density for these nuclei. The level densities are displayed in Figs. 5.1 and 5.2 for ^{163}Dy and ^{164}Dy, respectively. At low excitation energy a step-like structure is observed for ^{164}Dy. Similar structures are observed in several rare earth isotopes, in particular for even-even nuclei. The discrete levels below the plateau located beneath 1 MeV of excitation energy are caused by rotational modes of the nucleus. The plateau indicates that there are no new accessible levels within that energy region. In the ground state all the protons and neutrons are coupled together with other protons and neutrons in time reversed orbitals, so-called Cooper pairs. As the energy increases the pairs will break up. The energy to break up proton pairs is calculated to be 1750 keV in^{164}Dy, and 1664 keV to break up neutron pairs, by evaluating

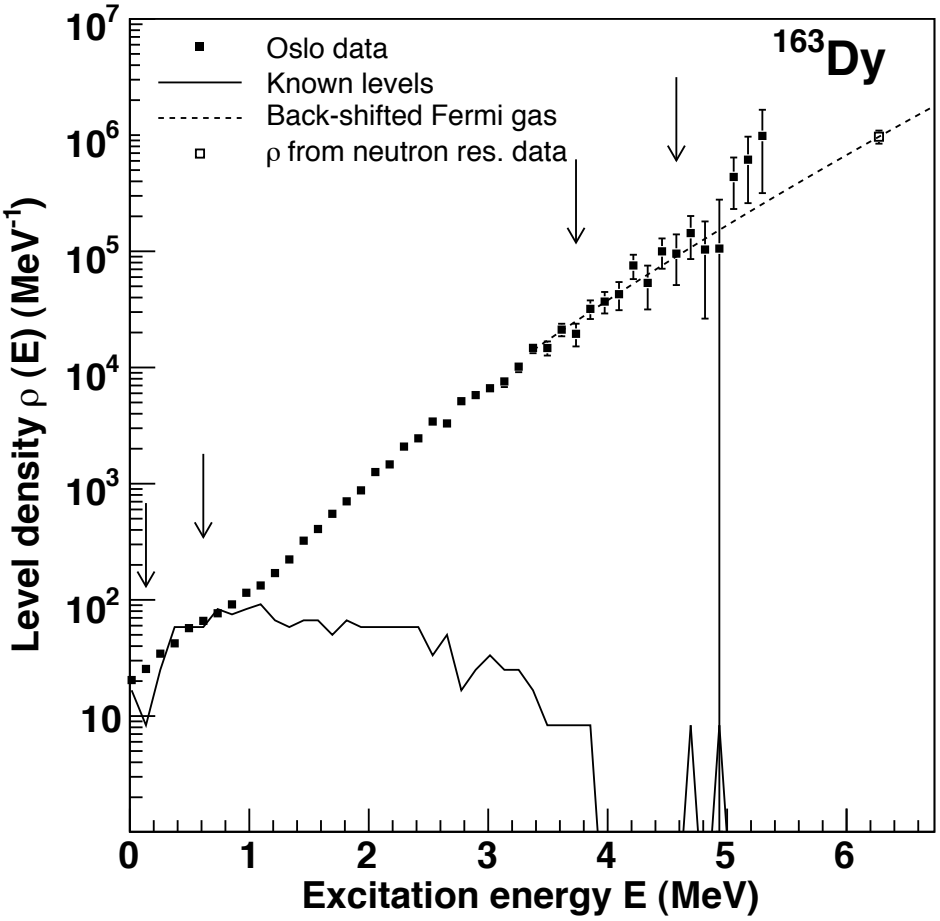

Figure 5.1: *Experimental level density for ^{163}Dy. The data points between the arrows are normalized to known levels at low excitation energy and to the level density at the neutron binding energy using an interpolation with the Fermi gas level density, as described in chapter 4.*

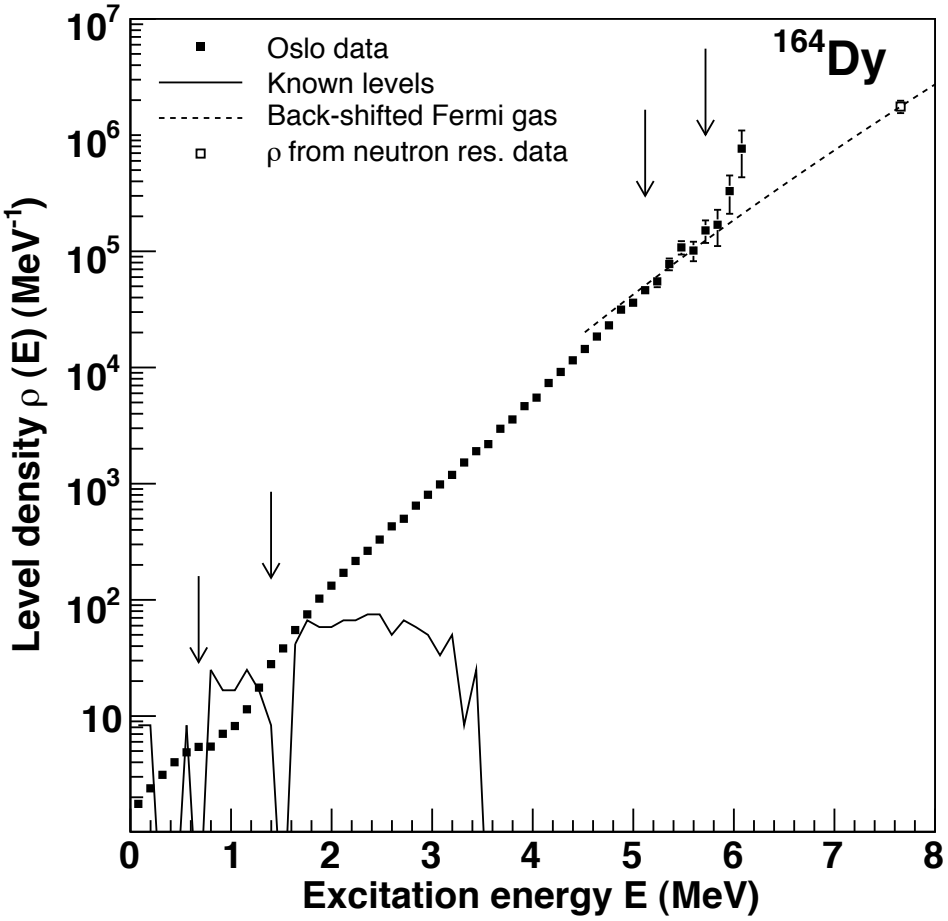

Figure 5.2: *Experimental level density for ^{164}Dy. The data points between the arrows are normalized to known levels at low excitation energy and to the level density at the neutron binding energy using an interpolation with the Fermi gas level density, as described in chapter 4.*

odd-even mass differences [40]. We observe in Fig. 5.2 that the level density for ^{164}Dy gains a steeper slope above approximately 1.6 MeV, this is interpreted as the first pair break-up. With two unpaired nucleons there are more configurations accessible and hence a higher level density is observed. Equivalently the energy needed to break up proton pairs in ^{163}Dy is 1322 keV, whereas the nucleus already has an unpaired neutron. However, due to a smearing effect of the valence neutron in ^{163}Dy we can not identify the breaking of Cooper pairs in this nucleus by studying the level density. With exception of the step structure at low energy in ^{164}Dy the level density in both nuclei increases smoothly. We observe that the level density in the even-odd ^{163}Dy nucleus is higher than in the even-even ^{164}Dy nucleus as a function of excitation energy. The even-odd nucleus has an uncoupled neutron in the ground state, and will have more quasi-particles as the energy increases and Cooper pairs start breaking up.

One can note that the error bars in both Figs. 5.1 and 5.2 increase as a function of excitation energy. This is due to less data accumulated for higher excitation energies. Simply because we only look at decay from the neutron binding energy down to the ground state, there are very few levels decaying to the levels corresponding to the last data points. At low excitation energy we have more counts and hence the level density can be determined with better precision.

5.2 Experimental thermodynamic properties

The thermodynamic properties are extracted by the use of statistical mechanics. The nucleus can be considered as an isolated system and one would therefore think that if reflects properties of the micro-canonical ensemble. However, the micro-canonical ensemble produces some controversial results where one can obtain negative temperatures and heat capacities. It is challenging for theoreticians to explain these negative values. Some prefer therefore to apply the canonical ensemble where one avoid this problem. In the following sections we will derive results from both ensembles. An obvious objection for using either of these ensembles is that they are designed to describe macroscopic systems, which do not apply to our systems consisting of 163 and 164 nucleons for ^{163}Dy and ^{164}Dy, respectively. However, because of the lack of a model that describes such small systems we choose to apply the current ensembles, but one must keep this in mind when interpreting the results. A comparison of the two ensembles is given at the end of this chapter.

5.3 Micro-canonical ensemble

5.3.1 Entropy

The entropy S is described through the following expression

$$S = \ln \rho(E) + S_0, \tag{5.1}$$

where we have set the Boltzmann's constant k_B equal to unity for simplicity. The level density is represented by $\rho(E)$ and S_0 is a constant. The third law of thermodynamics states that as the temperature tends to zero ($T \rightarrow 0$), so does the entropy ($S \rightarrow 0$). We can utilize this law when normalizing the entropy in ^{164}Dy. The even-even nucleus ^{164}Dy has only one accessible level in the ground state and we

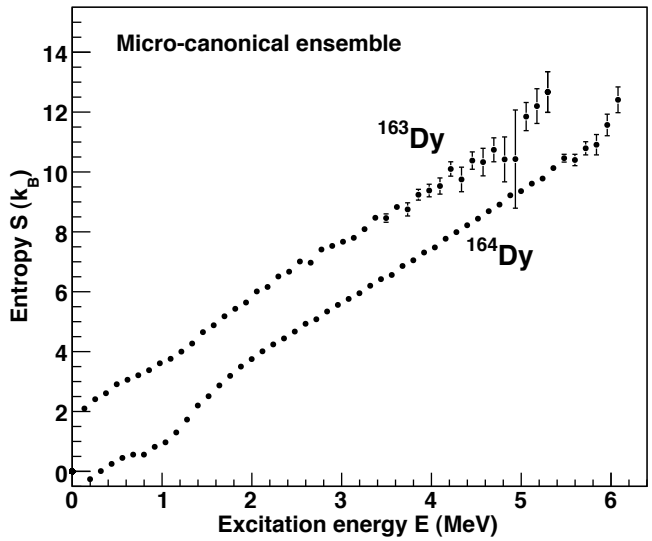

Figure 5.3: *Entropy for ^{163,164}Dy in the micro-canonical ensemble.*

therefore normalize the entropy to zero at zero excitation energy. Whereas the lowest lying states in the even-odd ^{163}Dy nucleus involve the excitation of one single particle state, and is interpreted as a single quasi-particle state. These states are rather close in energy to the ground state and cause the entropy for ^{163}Dy to have a finite value already at low temperature.

The entropies derived from the micro-canonical ensemble are given in Fig. 5.3, as a function of excitation energy. The entropies are, except for the error bars, identical in form to the level densities of Figs. 5.1 and 5.2 which are plotted in

logarithmic scale. This is as expected due to the relation $S \propto \ln\rho$. The shape of the entropy is therefore understood by using the same reasoning as in Sec. 5.1.

In macroscopic systems the entropy is considered an extensive quantity, that is a quantity that is proportional to the size of the system. However, for nuclei where the size of the system is small compared to the range of the strong interaction, this does not hold. Instead indications have been found that the entropy is an extensive function with respect to the number of quasi-particles [44]. In this case the entropy can be expressed as $S = nS_1$, where n is the number of quasi-particles and S_1 is the single quasi-particle entropy. This seems to be in agreement with our results, see Fig. 5.4 where the entropy difference between ^{163}Dy and ^{164}Dy is displayed. The entropy difference appears to be fluctuating around the mean value equal to 1.85 k_B in the energy region above 1.5 MeV, independent of excitation energy. This indicates that the entropy of the single quasi-particles is about $\sim$ 1.85 k_B. However, as the number of broken pairs increase every new broken pair will not contribute as much to the level density and hence to the entropy. We therefore expect that the entropies of the two nuclei will eventually coincide. Our results from the micro-canonical ensemble indicates that this happens far above 5 MeV of excitation energy, because the entropies does not approach each other in this energy region.

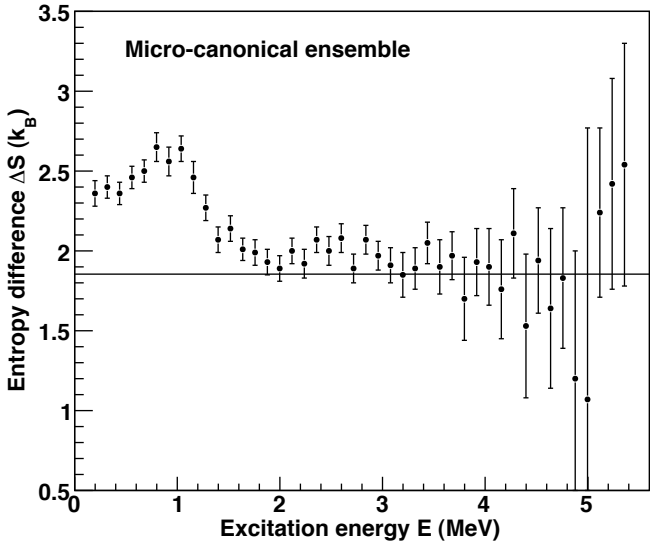

Figure 5.4: *Entropy difference between* ^{163}Dy *and* ^{164}Dy *in the micro-canonical ensemble. The solid line represents the average value found above an excitation energy of* 1.5 *MeV.*

5.3.2 Temperature

The temperature of the micro-canonical ensemble is obtained by taking the derivative of the entropy with respect to energy. Obviously the constant S_0 will cancel under derivation, however even small changes in the factor $\ln\rho$ will cause huge fluctuations. To limit the sensibility the derivation is performed by a least square fitting to a linear function over five bins, although we will loose some information by this smoothing. The results can be viewed in Figs. 5.5 and 5.6 for ^{163}Dy and ^{164}Dy, respectively. The error bars reflect the fluctuations of the derivation method and the statistical uncertainties which is generated because the system is very small. In both figures we observe a peak at low temperatures that needs commenting. We observe in Fig. 5.6 that the highest temperature in this peak exceeds the excitation energy of the nucleus. This is obviously not a physical property, but a result of trying to obtain the temperature in a region where there only exist a few levels. Above the energy regions corresponding to the first pair break-up

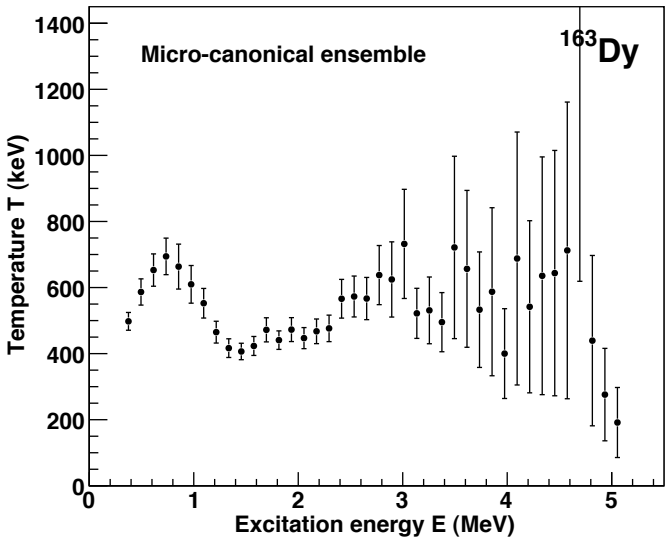

Figure 5.5: *Temperature for* ^{163}Dy *as a function of excitation energy in the micro-canonical ensemble.*

at ≈ 1.2 MeV and ≈ 1.6 MeV in ^{163}Dy and ^{164}Dy, respectively, the level density increases significantly and the temperatures above this point can be considered realistic. The negative slopes are caused by energy taken from the system in order to break up pairs, and hence the temperature decreases. However, relatively large uncertainties above the first break-up make it hard to determine in which regions

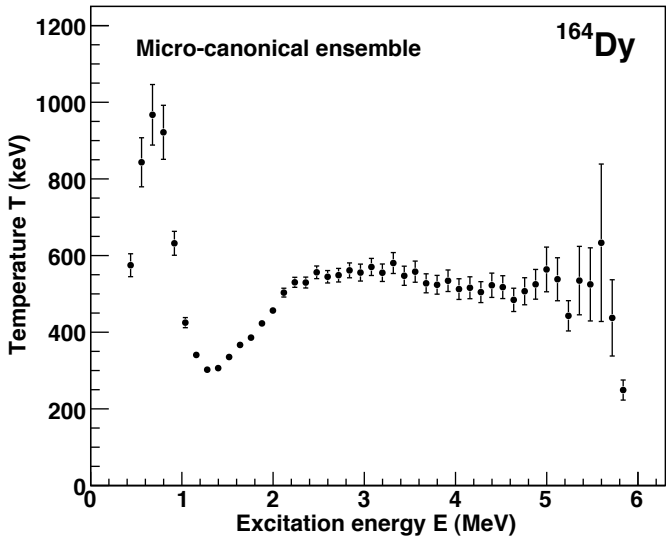

Figure 5.6: *Temperature for* ^{164}Dy *as a function of excitation energy in the micro-canonical ensemble.*

the temperature decrease.

5.3.3 Heat capacity

In the micro-canonical ensemble one obtains the heat capacity by taking the derivative of the temperature with respect to energy. Since the temperatures displayed in Figs. 5.5 and 5.6 have negative slopes in some regions, we will obtain negative values of the heat capacities, as seen in Figs. 5.7 and 5.8 for ^{163}Dy and ^{164}Dy, respectively. Interpreting these negative values is a controversial topic as discussed in [42, 43]. As described in the previous section the negative values can originate from the breaking of Cooper pairs.

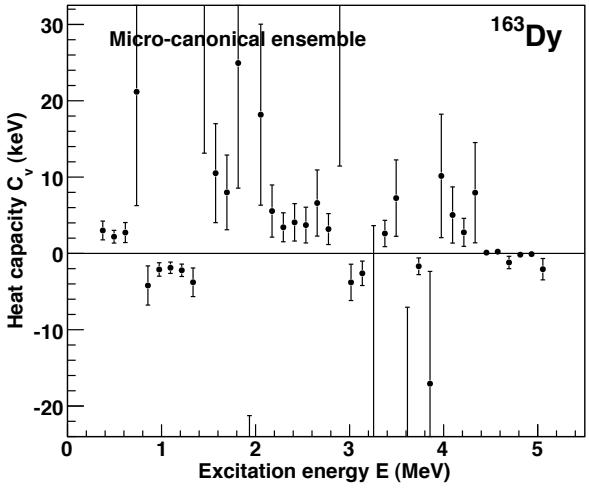

Figure 5.7: *Heat capacity for* ^{163}*Dy as a function of excitation energy in the micro-canonical ensemble.*

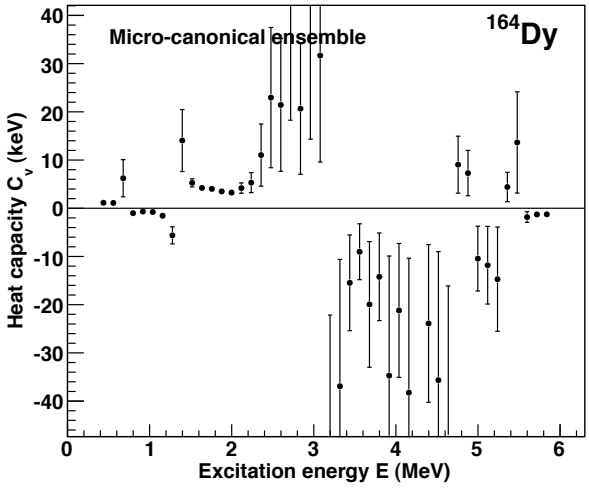

Figure 5.8: *Heat capacity for* ^{164}*Dy as a function of excitation energy in the micro-canonical ensemble.*

5.4 Canonical ensemble

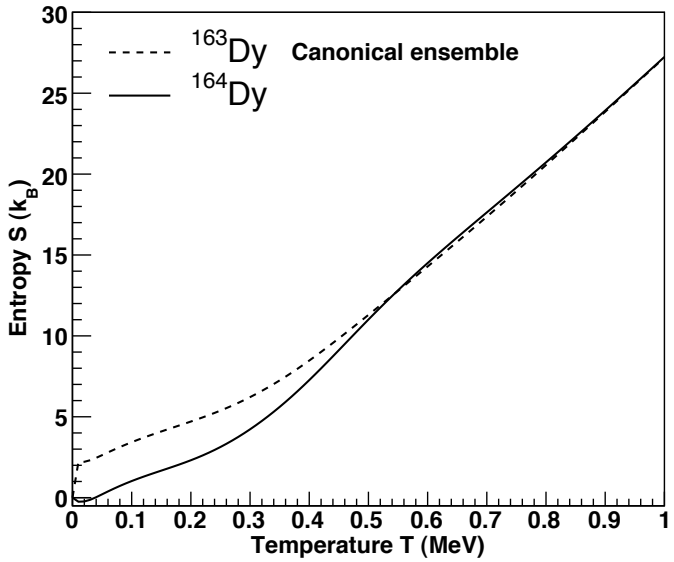

Figure 5.9: *Entropy for ^{163,164}Dy as a function of temperature in the canonical ensemble.*

5.4.1 Entropy

Due to the strong smoothing introduced by the transformation to the canonical ensemble as described in chapter 2, we do not observe clear transitions between the various quasi-particle regimes as we did in the micro-canonical ensemble, but only the transition where all pairing correlations are quenched as a whole. The results for the entropies in the canonical ensemble for ^{163,164}Dy are given in Fig. 5.9. We observe a clear entropy difference between the two nuclei at temperatures below $T \leq 0.5-0.6$ MeV, where the even-odd ^{163}Dy nucleus has the highest entropy. For the lowest temperature we observe an entropy difference of $\approx 2\ k_B$ between the two nuclei, which is of the same order as in the micro-canonical ensemble. At around $T = 0.5-0.6$ MeV the entropy of the even-odd and even-even system approach each other, this corresponds to an average excitation energy of $\langle E \rangle = 2.6-4.2$ MeV in ^{163}Dy, and $\langle E \rangle = 3.4-5.3$ MeV in ^{164}Dy. Above this region the entropy curves coincide and display almost identical behavior. Also the entropies of ^{161,162}Dy coincide at approximately the same excitation

energy [44], and the form of these entropies are very similar to what we observe in ^{163,164}Dy. This is understood because the pairing plays a less significant role as the level density becomes high, as already mentioned in Sec. 5.3.1. However, in the micro-canonical ensemble indications where found that the effect of pairing does in fact play a role even far above 5 MeV of excitation energy. The different results are partly due to the smoothing introduced in the canonical ensemble, and partly because we are dealing with two different physical systems.

We observe in Fig. 5.9 that the entropies are given up to a temperature of 1 MeV, this correspond to an excitation energy of 15 MeV. It has been obtained by extrapolating with the Fermi gas model above the neutron binding energies. A similar extrapolation has been performed for the energies and heat capacities in the canonical ensemble. These will be discussed in the next sections.

5.4.2 Energy

The average excitation energies $\langle E \rangle$ behave smoothly as a function of temperature, see Fig. 5.10. We observe that the ^{164}Dy nucleus has a higher $\langle E \rangle$ than the neighboring ^{163}Dy nucleus as a function of temperature. In Ref. [45] a model based on the canonical ensemble theory was applied to performed calculations for nuclei around ^{162}Dy. It was found that even-even, odd-even/even-odd and odd-odd systems have different excitation energies at one and the same temperature, where the even-even system requires the highest $\langle E \rangle$ value. This is also confirmed by experimental data, for example in Ref. [4] for ^{160,161}Dy.

5.4.3 Heat capacity

We observe the characteristic S-shape of the heat capacity of ^{164}Dy in Fig. 5.11 which is interpreted as a fingerprint of phase transition. The S-shape is much weaker for ^{163}Dy, displayed in the same figure. In Ref. [46] two different critical temperatures were discovered in the canonical ensemble using the method discussed in Ref. [47, 48]. The lowest critical temperature is explained by the first break up of Cooper pairs. The second critical temperature is due to the continuous melting of Cooper pairs at higher excitation energies. We see a significant increase in the heat capacity around temperature $T \approx 0.45$ MeV in the ^{164}Dy nucleus, which correspond to the first critical temperature. This first contribution is strongest for ^{164}Dy because this is an even-even nucleus and thus the first broken pair represents a large and abrupt step in the level density and thereby a large contribution to the heat capacity. The second critical temperature can be observed at about $T \approx 0.6$ MeV. The second critical temperature agrees with the region where the entropy curves coincides, see Fig. 5.9. Similar features for the heat capacity as discussed here are observed for ^{160,161}Dy [4].

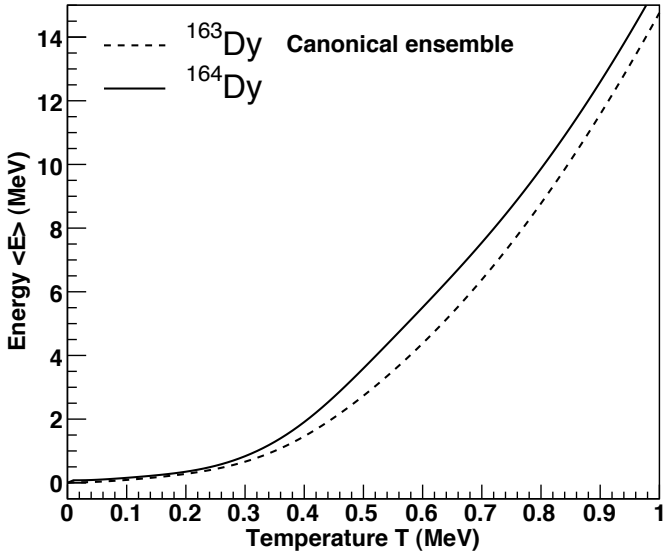

Figure 5.10: *Average excitation energy for ^{163,164}Dy as a function of temperature in the canonical ensemble.*

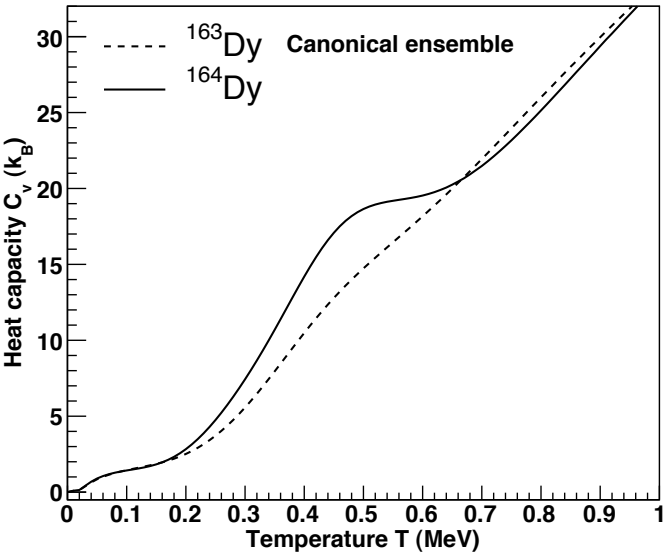

Figure 5.11: *Heat capacity for ^{163,164}Dy as a function of temperature in the canonical ensemble.*

5.5 Comparison of the ensembles

In the thermodynamic limit, that is when the number of particles in the system approach infinity, the micro-canonical and canonical ensemble should produce the same results. Our results show that we are clearly far away from the thermodynamic limit. When comparing the entropies of the two ensembles we observe that the importance of pair breaking above approximately 2.6 MeV of excitation energy for ^{163}Dy and 3.4 MeV of excitation energy for ^{164}Dy, can not be understood by studying the entropies of the canonical ensemble. However, by investigating the heat capacities in the canonical ensemble we get valuable information about phase transitions. The nucleus is a very small system and we have shown that the single quasi-particles in the low energy region which is under study here, have strong influence on the thermodynamic properties. These properties do best come to light when applying the micro-canonical ensemble rather than the canonical ensemble, which only gives average properties. In this sense we obtain more information when employing the micro-canonical ensemble. Another strong objection against using the canonical ensemble to describe the nucleus is that the system is assumed to be in contact with a heat bath. What this heat bath could be is hard to account for because the nuclear force has a very short range, and the nucleus does normally not share its excitation energy with its surroundings.

It is clear that neither of the ensembles are ideal to describe a system like the nucleus, however it would be fair to conclude that the micro-canonical ensemble seems to be the most suited one.

Chapter 6

Experimental results on the γ-ray strength function

In this chapter we will examine the results obtained for the γ-ray strength function. The most important contributions to the γ-ray strength function, in the low energy region, are thought to be the GEDR, the GMDR and the 3 MeV pygmy resonance. In the following we will fit models for these resonances to the experimental data points and compare with the results found for ^{160,161,162}Dy. In Sec. 6.3 and 6.4 we will discuss the results in light of what has been found through the two-step cascade (TSC) method.

6.1 The predicted γ-ray strength function fitted to experimental data

The total predicted γ-ray strength function is fitted to the experimental data points. The predicted γ-ray strength function can be described by

$$f = \kappa(f_{E1} + f_{M1}) + f_{py}, \tag{6.1}$$

where κ is a normalization constant, and f_{E1}, f_{M1} and f_{py} are functions representing the contributions from the GEDR, GMDR, and the pygmy resonance, respectively. They are each characterized by their strength, width, and centroid as described in chapter 2. We perform the fit to the experimental data points through a least square method where the normalization constant κ in addition to the strength, width and centroid of the pygmy resonance are used as free parameters. The GEDR and GMDR parameters are taken from the systematics of Ref. [19], and are listed in Tables 6.1 and 6.2, respectively.

The KMF model describing the GEDR is temperature dependent. We assume that the temperature is constant and found that the temperature of $T = 0.3$ MeV

provides the best fit to the experimental data. The results are displayed in Figs. 6.1 and 6.2 for ^{163}Dy and ^{164}Dy, respectively. The solid line in the figures gives the total predicted strength and the points represent the experimental data. In Fig. 6.1 we have a very good fit to the experimental points for ^{163}Dy , there is however a region around 5 MeV which does not fit well with the predicted strength. In the next section a different fit is applied to include this area.

We observe that the points close to the neutron binding energy in both nuclei have great uncertainties and do not follow the predicted strength. These data are a result of direct decay to the ground state and the first excited states from states at the neutron binding energy. The statistics in this region are so low that we can not treat the strength function for such energies with certainty.

We see from Fig. 6.2 that the strength function follows the total predicted strength nicely around the pygmy resonance in ^{164}Dy. Above this point the experimental points show a significantly higher strength than the predicted strength. Similar features have been observed in other nuclei, among these ^{116,124}Sn [49] and ^{208}Pb [50] through (γ,γ') experiments. In these nuclei the structure is thought to be governed by the so-called skin oscillation[1]. This is an E1 mode of the nucleus first predicted by van Isacker [51] and Chambers [52]. It is located in the excitation energy region of $6-10$ MeV, in stable nuclei [53]. The mode has been observed in nuclei with a high neutron to proton ratio N/Z. It is interpreted as an out of phase oscillation of the neutron enriched periphery of the nucleus versus the proton and neutron core [51, 52]. It is also observed in the nuclei ^{116,117}Sn in an experiment performed at the OCL through the reactions, $(^3\mathrm{He},\alpha)$ and $(^3\mathrm{He},^3\mathrm{He}')$, respectively. Although, the study of ^{116,117}Sn is ongoing and not yet published. Dysprosium nuclei have a higher neutron excess than ^{116,117}Sn, with a neutron to proton ratio between $N/Z = 1.36-1.48$ for the stable isotopes. It is therefore likely that the same oscillation can take place in these nuclei. Due to the lower binding energy in ^{163}Dy, we do not have experimental data above ≈ 6 MeV and can not observe the same effect in our extracted strength function.

A list of the 3 MeV pygmy resonance parameters and normalization constants is given in Table. 6.3. In Table. 6.4 the same parameters are displayed for ^{160,161,162}Dy. When comparing the results we see that the width of the pygmy resonance in ^{163,164}Dy coincides with what is measured for ^{160,161,162}Dy by use of the same method. However, we do observe a higher strength in the ^{163,164}Dy nuclei, and the centroids are located at slightly higher energies.

[1] Also referred to as the pygmy dipole resonance (PDR).

Nucleus	$E_{E1,1}$ (MeV)	$\sigma_{E1,1}$ (mb)	$\Gamma_{E1,1}$ (MeV)	$E_{E1,2}$ (MeV)	$\sigma_{E1,2}$ (mb)	$\Gamma_{E1,2}$ (MeV)
^{163}Dy	12.10	208.9	3.04	16.13	208.9	5.27
^{164}Dy	11.99	210.4	2.99	16.19	210.4	5.31

Table 6.1: *Parameters used in the KMF model for the GEDR for* ^{163,164}Dy.

Nucleus	E_{M1} (MeV)	σ_{M1} (mb)	Γ_{M1} (MeV)
^{163}Dy	7.50	0.84	4.00
^{164}Dy	7.49	0.86	4.00

Table 6.2: *Lorentz parameters used for the GMDR for* ^{163,164}Dy.

Nucleus	E_{py} (MeV)	σ_{py} (mb)	Γ_{py} (MeV)	κ
^{163}Dy	3.25(15)	0.70(17)	0.91(21)	1.89(16)
^{164}Dy	3.31(4)	0.50(3)	1.19(10)	1.49(4)

Table 6.3: *Fitted 3 MeV pygmy resonance parameters and normalization constants.*

Reaction	E_{py} (MeV)	σ_{py} (mb)	Γ_{py} (MeV)	κ
$(^3\mathrm{He},\alpha)^{160}$Dy	2.63(17)	0.33(7)	1.57(40)	0.95(12)
$(^3\mathrm{He},\alpha)^{161}$Dy	2.68(8)	0.44(5)	1.26(19)	1.34(10)
$(^3\mathrm{He},^3\mathrm{He}')^{161}$Dy	2.80(5)	0.43(3)	1.26(11)	1.30(5)
$(^3\mathrm{He},\alpha)^{162}$Dy	2.69(14)	0.36(7)	1.32(31)	0.96(11)
$(^3\mathrm{He},^3\mathrm{He}')^{162}$Dy	2.59(5)	0.37(2)	1.36(14)	0.84(4)

Table 6.4: *Fitted 3 MeV pygmy-resonance parameters and normalization constants for* ^{160,161,162}Dy*, taken from Ref. [4].*

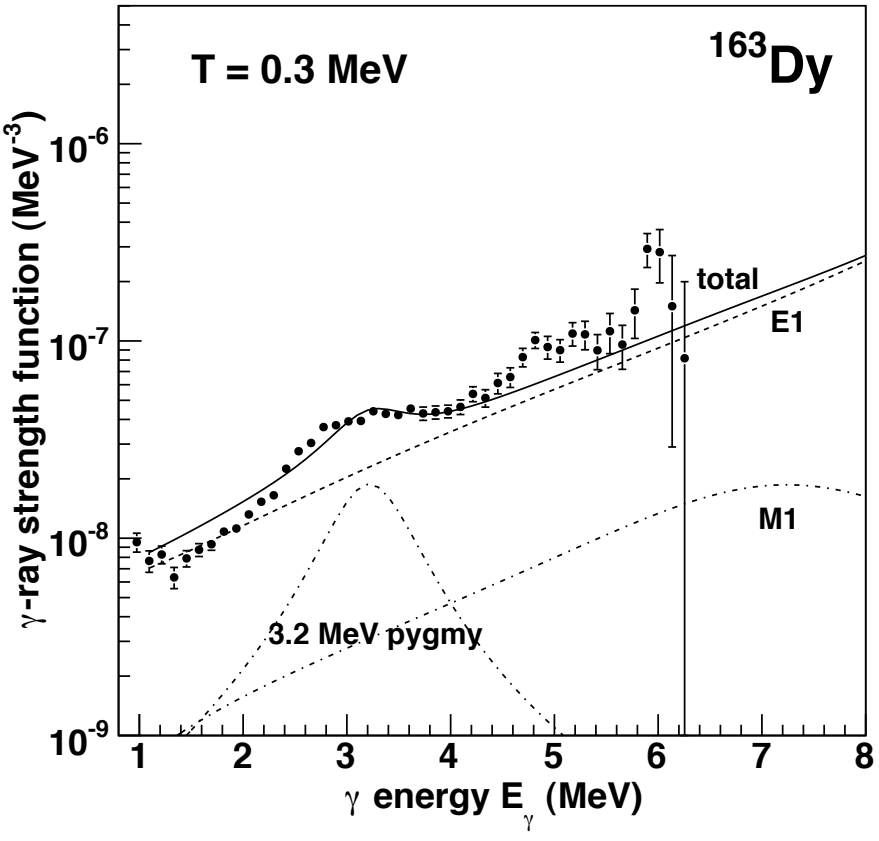

Figure 6.1: *The γ-ray strength function for ^{163}Dy. The solid line represents the predicted strength made up by the tail of the GEDR, the 3 MeV pygmy resonance and the GMDR. The temperature is set to $T = 0.3$ MeV.*

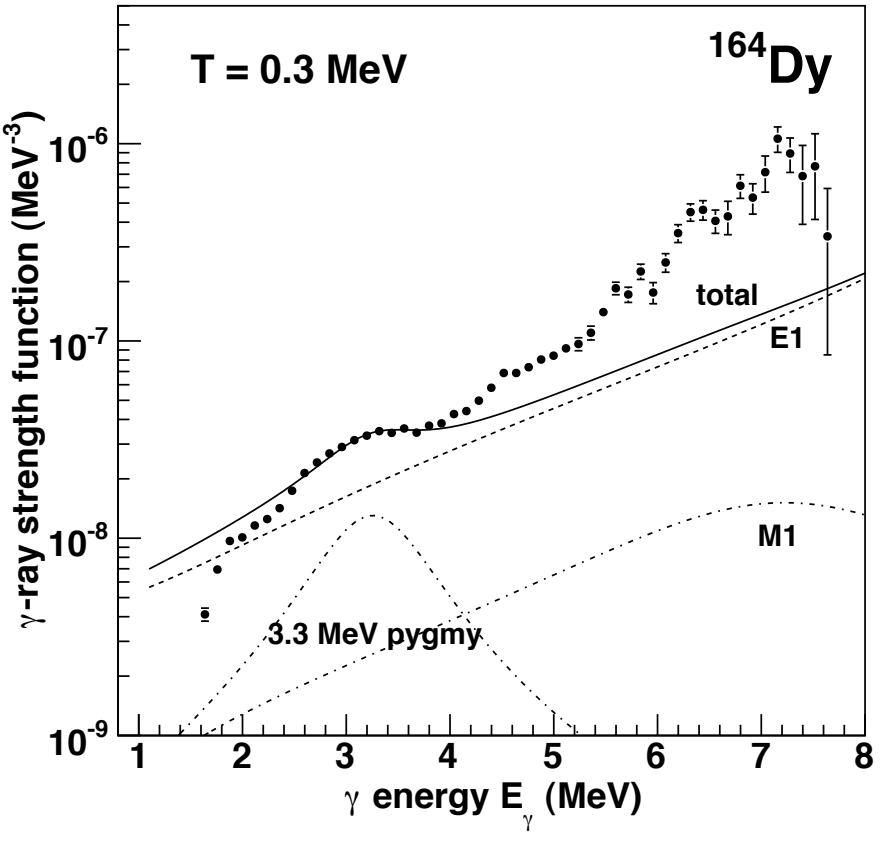

Figure 6.2: *The γ-ray strength function for ^{164}Dy. The solid line represents the predicted strength made up by the tail of the GEDR, the 3 MeV pygmy resonance and the GMDR. The temperature is set to $T = 0.3$ MeV.*

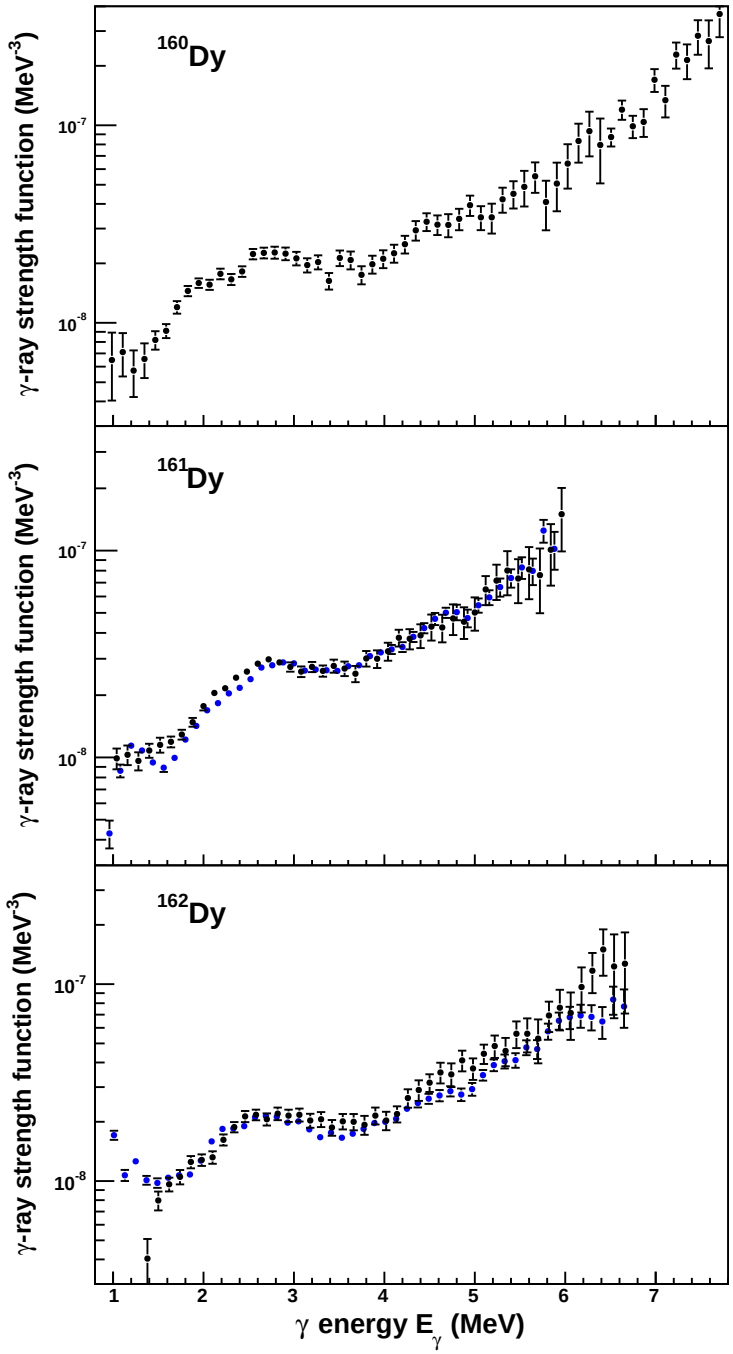

Figure 6.3: *The γ-ray strength functions of ^{160,161,162}Dy. The black and blue circles are measured with the (^{3}He,α) and (^{3}He,^{3}He′) reactions, respectively. The data are taken from Ref. [4].*

6.2 Including one extra Lorenzian function in the predicted γ-ray strength function

Previously, one has predicted only one pygmy resonance located at around 3 MeV. However, we observe in addition what appears to be a non statistical region at about 5 MeV, both for ^{163}Dy and ^{164}Dy. When comparing to dysprosium nuclei studied in the past, see Fig. 6.3, one observes the same feature, although not as pronounced as in the present strength functions. The previous experiments on dysprosium at the OCL collected far less data than for this experiment. It might therefore be that the strength functions of ^{160,161,162}Dy would be more similar to what we observe in ^{163,164}Dy if the statistics were better.

The strength functions have been fitted with one additional Lorentzian function, similar to the one used to fit the 3 MeV resonance, to include the extra strength found around 5 MeV. The results can be viewed in Figs. 6.4 and 6.5 for ^{163}Dy and ^{164}Dy, respectively. We observe that the new fit follows the experimental data points surprisingly well for the ^{163}Dy nucleus. A substantial improvement is also obtained for the ^{164}Dy nucleus. The origin of this extra strength is however uncertain. At present there are two known collective modes which result in pygmy resonances in the energy region under consideration here. One is the well established M1 pygmy resonance located around 3 MeV, and the other is the E1 skin oscillation, as described in Sec. 6.1, the later is located at energies above 5 MeV. Further investigation is therefore required to find the origin of the extra strength.

The parameters used to describe the pygmy resonances are given in Table 6.5. The parameters used for the GEDR and the GMDR are the same as in the previous fitting.

Nucleus	$E_{py,1}$ (MeV)	$\sigma_{py,1}$ (mb)	$\Gamma_{py,1}$ (MeV)	$E_{py,2}$ (MeV)	$\sigma_{py,2}$ (mb)	$\Gamma_{py,2}$ (MeV)	κ
^{163}Dy	3.15(11)	0.82(16)	0.91(17)	5.0	2.6	1.2	1.37(16)
^{164}Dy	3.30(6)	0.49(5)	1.05(11)	4.9	1.7	1.1	1.33(5)

Table 6.5: *Fitted 3 MeV pygmy resonance parameters and normalization constants, when including two pygmy resonances. The parameters for the resonance located around 5 MeV were set constant during the fitting.*

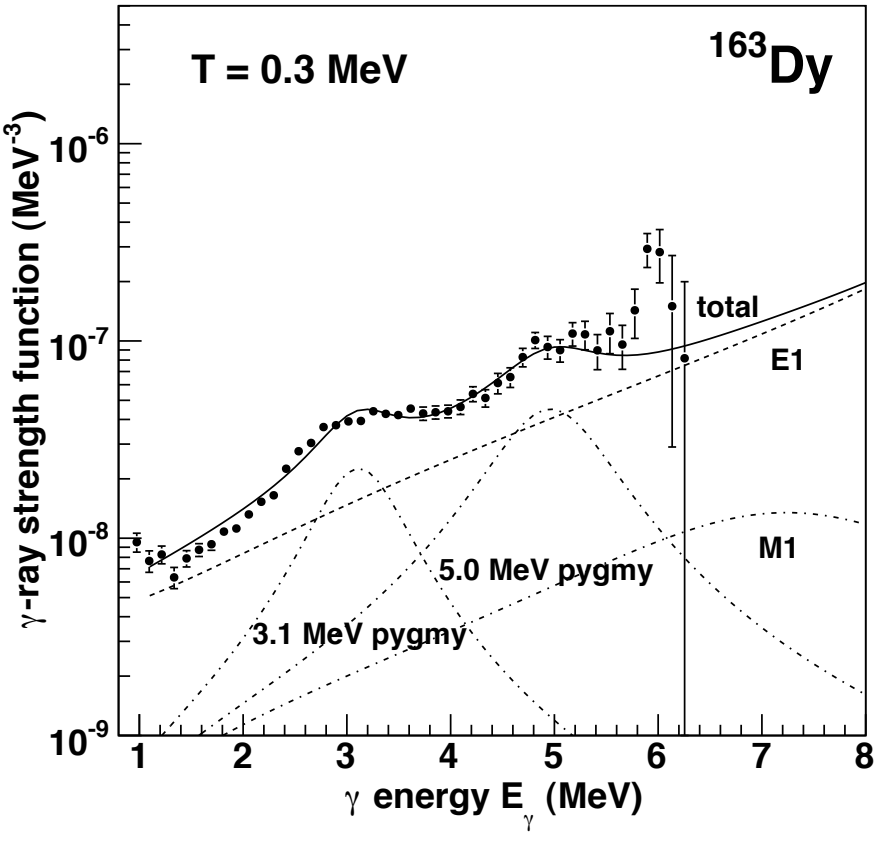

Figure 6.4: *The γ-ray strength function for ^{163}Dy. The solid line represents the total strength made up by the tail of the GEDR, two pygmy resonances and the GMDR. The temperature is set to $T = 0.3$ MeV.*

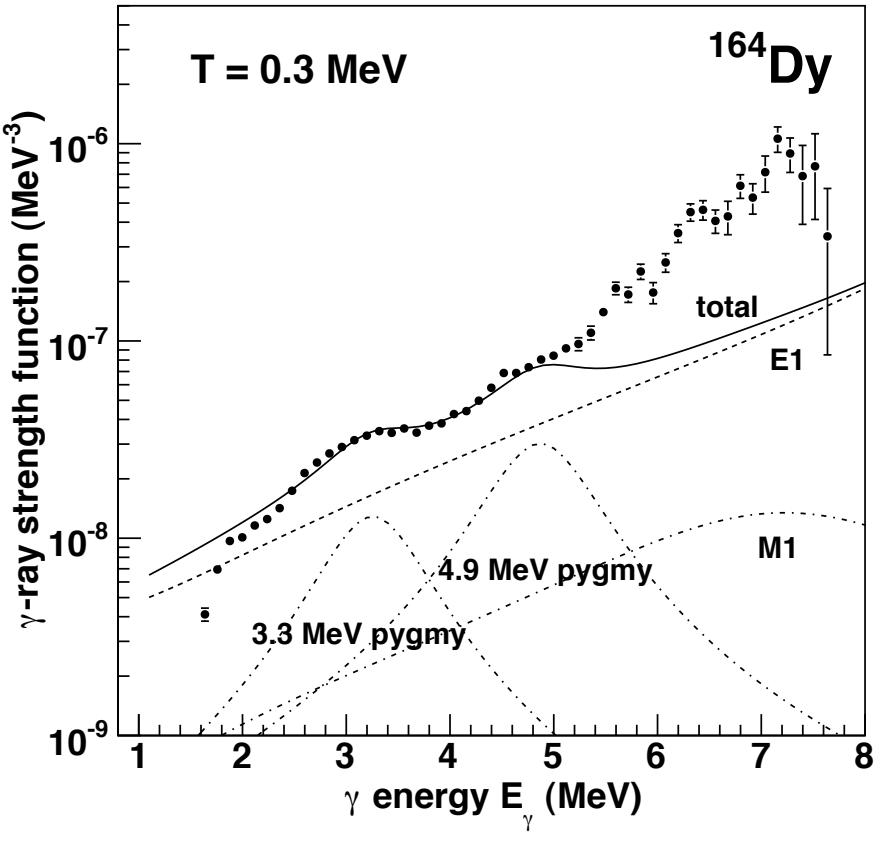

Figure 6.5: *The γ-ray strength function for ^{164}Dy. The solid line represents the predicted strength made up by the tail of the GEDR, two pygmy resonances GMDR. The temperature is set to $T = 0.3$ MeV.*

6.3 Comparing with results obtained from the two-step cascade method

The nucleus ^{163}Dy has been studied by use of the so called two-step cascade (TSC) method. The TSC method is a sum-coincidence method were only two γ-rays are involved in the cascade. The sum-coincidence method was first proposed by A. M. Hoogenboom in 1958 [54]. Excited nuclei usually decay through different cascades of γ-rays starting at one single level and ending at the ground state. The key property exploited in this method is that the total energy involved in the different cascades is the same given that the initial and final level in the cascades is the same in the nuclei. The γ-rays involved in a cascade are measured in coincidence with scintillation detectors. Later the technique was modified for germanium detectors by the Dubna group [55]. If the detectors have the same energy calibration, the sum of their output pulses are proportional to the total energy involved in the cascade, assuming that all the energy is absorbed in the detectors.

The experiment for studying ^{163}Dy was performed at the Řeš LWR-20 reactor. The coincidence setup consisted of two HPGe detectors with an efficiency of 30%. A beam of thermal neutrons was used and the reaction $^{162}\mathrm{Dy}(\mathrm{n},\gamma)^{163}\mathrm{Dy}$ was studied. Through this setup one measures three quantities: the deposited γ -ray energies in the detectors, $E_{\gamma 1}$ and $E_{\gamma 2}$, and the detector time difference Δt. These data are used to create a two-step γ cascade (TSC) spectrum. This spectrum contains the energy distribution of primary and secondary γ-rays that belong to all two-step cascade γ-rays that initiate at the neutron capturing state and terminate at a prefixed "terminal" level f in the product nucleus [56]. The background is subtracted by a method described in Ref. [5]. Through Monte Carlo simulations the level density and γ-ray strength function are produced according to Ref. [57].

One of the main motivations for doing our experiment was to investigate if the form of the γ-ray strength function is reaction dependent. The reason for suspecting this is that before our experiment one had measured a width of the pygmy resonance in ^{163}Dy to be 0.6 MeV [3], using the TSC method, which is about half of the value measured for other dysprosium isotopes by use of the Oslo method. The present analysis indicates that the width of the pygmy resonance is in fact reaction dependent. One parameter that differs significantly for the two experiments is the angular momentum transferred to the excited nucleus, this will be looked into in the following section.

6.4 Transferred angular momentum

In the TSC experiment thermal neutrons were used. Thermal neutrons have an energy of only around 0.025 eV, the spin transferred can therefore be neglected. The

angular momentum transferred in the Oslo experiment will be calculated in the following. When calculating spin transfer accurately on a system like a nucleus, one should apply quantum mechanics reaction theory. However, we will use classical mechanics and thereby not take into consideration the wave properties of the particles. One should therefore note that the values calculated in the following are not exact, but an indication of the real value. The angular momentum is given by the equation

$$|\vec{L}| = |\vec{r} \times \vec{p}| = r m_p v_p \sin\theta, \tag{6.2}$$

where m_p and v_p corresponds to the mass and velocity of the projectile, respectively, θ equals the angle between the position vector $\vec{r}$ and the vector $\vec{p}$ which represents the momentum of the projectile. The size of $\vec{r}$ is given by r and corresponds to the distance from the projectile to the core of the target nucleus. If we assume that the projectile hits the target nucleus with its center of mass at the edge of the target, the radius can be set equal to the radius of the target nucleus, expressed as $r = R_t = r_0 A_t^{1/3}$, where $r_0 = 1.25$ fm and A_t is the mass number of the target nucleus. Further, the velocity v of the ejectile can be calculated through the relativistic expression

$$E_p = \frac{m_p c^2}{\sqrt{1 - v^2/c^2}}, \tag{6.3}$$

where E_p is the kinetic energy of the projectile, and c represents the speed of light. Solving with respect to velocity yields,

$$v = c\sqrt{1 - \left(\frac{1}{\frac{E_p}{m_p c^2} + 1}\right)^2}. \tag{6.4}$$

Combining Eqs. (6.3) and (6.4) we obtain the following expression for the angular momentum transferred to the nucleus:

$$\left|\vec{L}\right| = r_0 A_t^{(1/3)} m_p c \sqrt{1 - \left(\frac{1}{\frac{E_p}{m_p c^2} + 1}\right)^2} \sin\theta. \tag{6.5}$$

In the present experiment the projectiles used were ^{3}He particles with a mass of 2809 MeV/c^2 and an energy of 38 MeV. The maximum angular momentum $L_{\max}$ transfer is obtained when the ejectile is emitted tangential to the nuclear surface and in the opposite direction of the rotation of the system [29]. At maximum transfer we have $\theta = 90^\circ$. However, the average value of the transferred angular momentum $\langle L \rangle$ is about half of the maximum value [29], this corresponds to

Projectile	E_p (MeV)	$\langle L \rangle$ ($\hbar$)	$L_{\max}$ ($\hbar$)
^{3}He	38	7.9	15.8
p	15	2.9	5.7

Table 6.6: *Angular momentum transferred from the projectile to the target nucleus, for* ^{3}He *and p projectiles.*

$\theta = 30^\circ$. Angular momentum calculated for the Oslo experiment is given in Table 6.6. In the same table it is displayed angular momentum transferred with a beam of 15 MeV protons, with a mass of 938 MeV/c^2. In april 2008 an experiment was performed at the OCL where ^{163}Dy was excited through the reaction $^{163}\mathrm{Dy}(\mathrm{p},\mathrm{p}')^{163}\mathrm{Dy}$. The beam used consisted of 15 MeV protons, we observe from Table 6.6 that this reaction would cause the average angular momentum that transferred to equal 2.9 $\hbar$. This is significantly less than the 7.9 $\hbar$ which is the average transferred angular momentum with the present experiment. Through the (p,p') experiment one could hopefully determine if the angular momentum influences the width of the 3 MeV pygmy resonance.

Chapter 7

Summary and outlook

7.1 Summary and conclusions

This thesis has dealt with extracting the level density, thermodynamic properties and the γ-ray strength function of ^{163,164}Dy by using the Oslo method. Through this method the distribution of the first γ-rays emitted in the decay cascades is found, which enables us to apply the Brink-Axel hypothesis to derive the above mentioned quantities. Both the level density and the γ-ray strength function are indispensable to characterize a nucleus in the quasi-continuum. Also, they are especially important when describing nuclear reactions.

The level density and thermodynamic results extracted exhibit characteristic features found for rare earth nuclei. The ^{163,164}Dy nuclei are medium heavy, mid-shell nuclei with a corresponding high level density. The even-odd system displays an overall higher level density than the even-even nucleus. This is due to the extra valence neutron which results in an approximate constant entropy difference in the quasi-continuum region. In the thermodynamic properties derived from the micro-canonical ensemble we observe distinct structures related to breaking of Cooper pairs. The canonical ensemble provides information about phase transitions. Although there are theoretical challenges when calculating the properties from the micro-canonical ensemble, we can conclude that this ensemble is the most appropriate to apply when describing a nucleus.

Interpreting the form of the γ-ray strength function is not as obvious as in the case of the level density. We observed a high strength in ^{164}Dy close to the neutron binding energy. This might be a result of skin oscillation. We found that the width of the 3 MeV pygmy resonance coincides with what is previously measured by use of the same method in other dysprosium isotopes. It does not agree with what has been found through the TSC method. Both the Oslo method and the TSC method are considered as reliable methods. Based of this we can conclude that it seems

as if the width of the 3 MeV pygmy resonance is reaction dependent. In addition, we observed what appears to be a second resonance located at around 5 MeV, this sheds new light on an earlier presumed statistical region. The extra strength in this region might also be seen in previous OCL data on other dysprosium isotopes. When performing a fit to the experimental data points for this new resonance where a similar Lorantzian function as for the 3 MeV resonance is included in the predicted strength function, we obtained a surprisingly good fit.

7.2 Outlook

Further investigations have to be performed in order to determine the origin of the extra strength at around 5 MeV as well as to determine if the high strength close to the binding energy in ^{164}Dy is in fact due to the skin oscillation. At present it is not fully understood why the OCL measurement and the TSC results differ when it comes to the width of the 3 MeV pygmy resonance. One factor that might influence the width of the pygmy resonance is the angular momentum transferred from the projectile to the target nucleus. Already new data have been collected at the OCL where ^{163}Dy was excited through the reaction (p,p'), which introduces less angular momentum than the reactions utilized in this work. If the width measured from the (p,p') reaction is smaller than the one measured by using a ^{3}He-beam, it will indicate that the angular momentum does play a role.

An improvement of the detector setup at the OCL is in progress. A highly efficient system of particle telescopes called the Silicon Ring (SiRi) is being developed. Each new telescope is formed as a trapeze, with an eight-fold segmented front detector in front of each of the eight end detectors. The telescopes are arranged in a ring and can be put in both forward and backward angles. The new system will cover a solid angle fraction of 6% of 4π. This will result in much higher statistics as well as improved energy resolution, since the segmented front detector allows a better angular resolution [58]. In the future we also aim for replacing the NaI(Tl) detectors of the CACTUS array with $LaBr_3$(Ce) detectors which has a 65% higher efficiency than the NaI(Tl) detectors, and almost three times the resolution [58]. For future experiments we will therefore be able to produce even more precise results.

Bibliography

[1] A. Schiller, L. Bergholt, M. Guttormsen, E. Melby, J. Rekstad, S. Siem , Nucl. Inst. Meth. **A 447** (2000) 498.

[2] A. Schiller, A. Voinov, E. Algin, J.A. Becker, L.A. Bernstein, P.E. Garrett, M. Guttormsen, R.O. Nelson, J. Rekstad, S. Siem, Phys. Lett. **B 633** (2006) 225.

[3] M. Krtička, F. Bečvář, J. Honzátko, I. Tomandl, M. Heil, F. Käppeler, R. Reifarth, F. Voss, K. Wisshak, Phys. Rev. Lett. **92** , 172501 (2004).

[4] M. Guttormsen, A. Bagheri, R. Chankova, J. Rekstad, S. Siem, A. Schiller, A. Voinov, Phys. Rev. **C 68** (2003) 064306.

[5] J. Honzátko, k. Konečný, I. Tomandl, J. Vacík, F. Bečvář, P. Cejnar, Nucl. Inst. Meth. **A 376** (1996) 434.

[6] H.A. Bethe, Phys. Rev. 50, 332 (1936).

[7] A. Gilbert, A. G. W. Cameron, Can. J. Phys. **43** (1965) 1446.

[8] T. von Egidy, H. H. Schmidt, A. N. Behkami, Nucl. Phys. **A 481** (1988) 189.

[9] T. von Egidy, Dorel Bucurescu, Phys. Rev. **C 72** , (2005), 044311, and Phys. Rev. **C 73** , (2006), 049901(E).

[10] H. Nakada, Y. Alhassid, Phys. Rev. Lett. **79** , (1997) 2939.

[11] Y. Alhassid, G. F. Bertsch, L. Fang, Phys. Rev. **C 68** , (2003) 044322.

[12] Y. Alhassid, S. Liu, H. Nakada, Phys. Rev. Lett. **99** , (2007), 162504.

[13] J. A. White, S. E. Koonin, D. J. Dean, Phys. Rev. **C 61**, 034303(R) (2000).

[14] A. C. Larsen, R. Chankova, M. Guttormsen, F. Ingebretsen, S. Messelt, J. Rekstad, S. Siem, N. U. H. Syed, S. W. degrd, T. Lönnroth, A. Schiller, A. Voinov, Phys. Rev. **C 73** , (2006), 064301.

[15] G. A. Batholomew, E. D. Earle, A. J. Fergusson, J. W. Knowles. M. A. Lone, Adv. Nucl. Phys. **7** , (1972), 229

[16] A. Schiller, M. Guttormsen, E. Melby, J. Rekstad, S. Siem, A. Voinov, Phys. Rev.**C 63** (2001) 044313.

[17] P. Axel, Phys. Rev. **126** (1962) 671.

[18] D. M. Brink, Ph. D. thesis, Oxford University (1955).

[19] RIPL-2: Handbook for calculations of nuclear reaction data, IAEA, Vienna, Report No. IAEA-TECDOC-1506 (2006).
URL: http://www-nds.iaea.org/RIPL-2/

[20] S. G. Kadmenskiĭ, V. P. Markushev, V. I. Furman, Yad. Fiz. **37** (1983) 277 [Sov. J. Nucl. Phys. **37** (1983) 165].

[21] A. Voinov, M. Guttormsen, E. Melby, J. Rekstad, A. Schiller, S. Siem, Phys. Rev. **C 63**, (2001), 044313.

[22] M. Guttormsen, Tech. Rep., UIO/PHYS/89-14, Institute of Physics, University of Oslo, (1989).

[23] S. Rezezedeh, Master‘s thesis, University of Oslo (2000).

[24] W. R. Leo, *Techniques for Nuclear and Particle Physics Experiments* (Springer-Verlag, 1993), pp. 24-25.

[25] A. Schiller, L. Bergholt, M. Guttormsen, E. Melby, S.Messelt, E. A. Olsen, J. Rekstad, S. Rezazadeh, S. Siem, T. S. Tveter, P. H. Vreim, J. Wikne, *Recent Upgrades and Performance of the CACTUS-Detector Array,* Tech. Rep., UIO/PHYS/98-02, Institute of Physics, University of Oslo, (1998).

[26] M. Guttormsen, T.S. Tveter, L. Bergholt, F. Ingebretsen, J. Rekstad, Nucl. Inst. Meth. **A 374** (1996) 371.

[27] M. Guttormsen, T. Ramsøy, J. Rekstad, Nucl. Inst. Meth. **A 255** (1987) 518.

[28] T. S. Tveter, M. Guttormsen, J. Rekstad, J. Kownacki, T. F. Thorsteinsen, Nuclear Physics **A 516** (1990) 1.

[29] M. Guttormsen, L. Bergholt, F. Ingebretsen, G. Løvhøiden, S. Messelt, J. Rekstad, T. S. Tveter, H. Helstrup, T. F. Thorsteinsen, Nuclear Physics **A 573** (1994) 130.

[30] L. Henden, L. Bergholt, M. Guttormsen, J. Rekstad, T. S. Tveter, Nuclear Physics **A 589** (1995) 249.

[31] A. Bohr, B. Mottelson, Nuclear Structure, Benjamin, New York, 1969, Vol. I, pp. 184-185.

[32] J. Rekstad, A. Henriquez, F. Ingebretsen, G. Midttun, B.Skaali,R. Øyan, J. Wikne, T. Engeland, T. F. Thorsteinsen, E. Hammaren, E. Liukkonen, Phys. Scr. T 5, (1983) 45.

[33] E. Andersen, H. Helstrup, G.Løvhøiden, T.F. Thorsteinsen, M. Guttormsen, S. Messelt, T.S. Tveter, M.A. Hofstee, J.M. Schippers, S.Y. van der Werf, Nuclear Physics **A 550** (1992) 235.

[34] S. Leoni, G. Benzoni, A. Bracco, N. Blasi, F. Camera, C. Grassi, B. Million, A. Paleni, M. Pignanelli, E. Vigezzi, O. Wieland, M. Matsuo, T. Dssing, B. Herskind, G.B. Hagemann, J. Wilson, A. Maj, M. Kmiecik, G. Lo Bianco, C.M. Petrache, M. Castoldi, A. Zucchiati, G. De Angelis, D. Napoli, P. Bednarczyk, D. Curien, Acta Physica Polonica **B 36** , (2005), 1121

[35] E. Ramakrishnan, A. Azhari, J. R. Beene, R. J. Charity, M. L. Halbert, P. -F. Hua, R. A. Kryger, P. E. Mueller, R. Pfaff, D. G. Sarantites, L. G. Sobotka, M. Thoennessen, G. Van Buren, R. L. Varner, S. Yokoyama, Phys. Lett. **B 383** , (1996), 252

[36] V. K. Sirotkin, Yad. Fiz. **43** (1986) 570 [Sov. J. Nucl. Phys. **43** (1986) 362].

[37] A. Schiller, E. Algin, L. A. Bernstein, P. E. Garrett, M. Guttormsen, M. Hjort-Jensen, C. W. Johnson, G. E. Mitchell, J. Rekstad, S. Siem, A. Voinov, W. Younes, Phys. Rev. **C 68** (2003) 054326.

[38] Data extracted using the NNDC On-Line Data Service from the ENSDF database. URL: http://www.nndc.bnl.gov/ensdf/

[39] G. Audi, A. H. Wapstra, Nucl. Phys.**A 595** (1995) 409.

[40] A. Bohr, B. Mottelson, *Nuclear Structure* (Benjamin, New York, 1969), Vol. I, pp. 169-171.

[41] J. Kopecky, M. Uhl, Phys. Rev. **C 41** (1990) 1941.

[42] E. Melby, M. Guttormsen, J. Rekstad, A. Schiller, S. Siem, Phys. Rev. **C 63** (2001) 044309.

[43] A. Schiller, M. Guttormsen, M. Hjort-Jensen, J. Rekstad, S. Siem, Phys. Rev. **C 66** (2002) 024322.

[44] M. Guttormsen, A. Bjerve, M. Hjort-Jensen, E. Melby, A. Schiller, S. Siem, A. Belić, Phys. Rev. **C 62** (2000) 024306.

[45] M. Guttormsen, M. Hjort-Jensen, E. Melby, J. Rekstad, A. Schiller, S. Siem, Phys. Rev. **C 64** (2001) 034319.

[46] M. Guttormsen, R. Chankova, M. Hjort-Jensen, J. Rekstad, S. Siem, A. Schiller, D. J. Dean, Phys. Rev. **C 68** (2003) 034311.

[47] J. Lee, J. M. Kosterlitz, Phys. Rev. Lett. **65** (1990) 137.

[48] J. Lee, J. M. Kosterlitz, Phys. Rev. **B 43** (1991) 3265.

[49] K. Govaert, F. Bauwens, J. Bryssinck, D. De Frenne, E. Jacobs, W. Mondelaers, L. Govor, V. Yu. Ponomarev, Phys. Rev. **C 57** , (1998), 2229.

[50] N. Ryezayeva, T. Hartmann, Y. Kalmykov, H. Lenske, P. von Neumann-Cosel, V. Yu. Ponomarev, A. Richter, A. Shevchenko, S. Volz, J. Wambach, Phys. Rev. Lett. **89** , (2002), 272501.

[51] P. van Isacker, M. A. Nagarajan, D. D. Warner, Phys. Rev. **C 45** (1992) R13.

[52] J. Chambers, E. Zaremba, J. P. Adams, B. Castel, Phys. Rev. **C 50** (1994) R2671.

[53] A. Zilges, M. Babilon, T. Hartmann, D. Savran, S. Volz, Prog. Part. Nucl. Phys. **55** (2005) 408.

[54] A. M. Hoogenboom, Nucl. Inst. Meth. **3** (1958) 57.

[55] S. T. Boneva, E.V. Vasilieva, Yu. P. Popov, A. M. Sukhovoj, V. A. Khitrov, Particles and Nuclei 22 (1991) 479.

[56] F. Bečvář, J. Honzátco, M. Kritčka, S. Pašić, G. Rusev, I. Tomand, Nucl. Inst. Meth. **B 261** (2007) 930.

[57] F. Bečvář, Nucl. Inst. Meth. **A 417** , (1998) 434.

[58] A. C. Larsen, PhD thesis, University of Oslo (2008).